Department of Precision and Microsystems Engineering

Metastructures in a sensor-actuator configuration: the practical issues in bandgap generation

Francesco Coatto

Report no : 2023.043
Coach : M. B. Kaczmarek
Professor : Dr. S.H. Hossein Nia Kani
Specialisation : Mechatronic System Design
Type of report : Master Thesis
Date : 17^{th} July 2023

Acknowledgements

For the purpose of graduating in the Master's program in High-Tech Engineering, with a specialisation in Mechatronic System Design, this work documents the process and results of my thesis project, officially marking the end of my academic journey at the Technical University of Delft.

I would like to thank my daily supervisor Marcin for his help and guidance throughout the entirety of the project. Indeed, his insightful comments and remarks were crucial in improving both the quality of my work and my critical thinking skills. On top of that, I also want to thank him for helping me be more confident about my knowledge and understanding of things, which has fostered greater independence and analytical thinking throughout the process. I will always be grateful for his patience, encouragement, and belief in my abilities.

I would also like to thank my senior supervisor, Hassan, for making his invaluable expertise, experience, and vast knowledge available to me throughout the project. His mentorship and insightful feedback have played a pivotal role in enhancing the quality of my work, especially in the final stages of the project. The bi-weekly meetings, apart from deepening my knowledge on multiple mechatronic-related topics, significantly helped me in improving both my communication and presentation skills, which I find are valuable ones to possess. I will forever be thankful to him for giving me the opportunity to work under his supervision, enriching my academic experience as well as my personal and professional growth.

Additionally, I would like to express my heartfelt gratitude to my family, friends, and girlfriend for their unwavering support and encouragement throughout this journey. Although they might not understand the technical contents of this document, I am sure they will recognise the effort, dedication, and passion that went into its creation.

I extend my gratitude to my fellow peers Aditya, Shiyu, Castor, and Maurits. Our weekly meetings, as we embarked on similar projects, proved to be a constant source of inspiration. The collaborative atmosphere allowed us to support one another, troubleshoot together, and share our expertise, particularly within the mechatronics lab. Most importantly, you contributed to making the whole process a pleasant experience.

Lastly, I wanted to thank the lab support and staff for allowing me to work in the Mechatronics lab at the 3ME faculty. Their support in providing me with all the necessary components I needed for building my experimental setup was crucial.

Francesco Coatto
Delft, July 2023

Abstract

Undesired vibrations are one of the most significant sources of error in any type of mechatronic system or component. The emerging field of elastic (locally resonant) metamaterials offers a viable solution to successfully suppress these by generating bandgaps in both resonant and non-resonant regions. In this thesis, metamaterials in a sensor-actuator configuration using piezoelectric transducers are employed to generate vibration attenuation regions in beam-like structures. The main contribution of this thesis consists in studying the practical issues involved in the experimental implementation of such metamaterial architectures, often overlooked in the literature. To this aim, parasitic dynamics such as time delay and RC roll-off characteristics of piezoelectric transducers are considered, and their influence on controller choice is evaluated. The research was conducted using full model simulations in SPACAR and an experimental setup. The RC roll-off characteristic of piezoelectric transducers was found to be significant in limiting the bandgap generation capabilities of the system in non-resonant regions. The reason for this was the added phase caused by the parasitic effect, which required a reduction in controller gain for stability and ultimately reduced the bandgap performance. This was not the case for resonant bandgaps, where the phase lead was compensated by the increase in gain at the resonance. This ultimately allowed for optimal resonant bandgaps to be generated and observed. Methods to compensate for such parasitic effects are proposed and suggestions on how to implement these to attain non-resonant bandgaps are made.

Contents

Chapter 1

Introduction

1.1 Motivation

Mechanical vibration is defined as a periodic process of oscillations with respect to an equilibrium point [1]. Undesired vibrations are one of the most significant sources of error in any type of mechatronic system or component. The detrimental effects of unwanted vibrations are particularly important in the precision industry, where these can significantly limit the performance of systems and in the worst cases cause failure [2]. For instance, in wafer stages for semiconductor lithography machines, undesired vibrations can cause misalignment of the wafer position, which can ultimately result in the failure of the production process.

Vibrations in mechatronic systems arise for a number of reasons. For instance, vibrations can be transmitted through direct forces acting on the base of a structure, such as the ground or a motion system. Alternatively, vibrations can be induced by transient excitations from nearby roads or human activities in the building. Furthermore, as lightweight materials become more prevalent, the structural damping of precision mechanisms decreases while their stiffness increases. This unfavourable combination amplifies the transmission of disturbances within these systems. Moreover, in recent years, the increasingly stringent demands on mechatronic systems, which require bandwidths to be pushed as high frequency as possible, have made the detrimental effects of vibrations in such systems further significant. Therefore, it is necessary for solutions to be adopted for these vibrations to be successfully suppressed.

One possible solution consists of active damping control. In the mechatronic industry, adding damping to a system can be beneficial to suppress its resonant modes. For instance, when operating in a vacuum environment the effects of damping are reduced, and hence this needs to be added artificially through damping control to suppress resonant vibrations. One common example of an active damping strategy in the literature is Direct Velocity Feedback (DVF) [3]. However, not all responses that ought to be controlled are resonant responses. In fact, active control of non-resonant vibrations is also important when considering external disturbances and their transmissibility.

For this, metamaterials present a more viable solution thanks to their ability to generate bandgaps, which are frequency ranges where the transmission of vibrations will approach zero. Metamaterials are specially engineered composites consisting of a small-scale repeated structure (called a unit-cell) that yields large-scale effective properties not found in nature. Examples include

negative refractive index [4] or negative effective modulus [5]. Indeed, a possible application for metamaterials in precision mechanisms lies in their ability to generate bandgaps.

Specifically, the emerging field of elastic (locally resonant) metamaterials has proven to be promising in generating low-frequency bandgaps based on the exceptional results conferred in the area of applied physics [6]. Here, bandgaps can be attained by incorporating resonators in the unit cells that form the metamaterial. In this configuration, at the resonator's natural frequency, most of the vibrational energy is absorbed internally, leaving only a limited amount to be transmitted to the structure. This absorption ultimately creates a vibration attenuation region, also known as a bandgap. Metamaterials using mechanical resonators such as tuned mass dampers (TMDs) in their constituent unit cells are known as mechanical metamaterials [7]. Alternatively, resonators can be generated electronically by using piezoelectric transducers in each unit cell. These are known as electromechanical (piezoelectric) metamaterials [8]. In this report, only the latter type will be analysed.

In piezoelectric metamaterials, shunt circuits are commonly implemented in the unit cells [9]. These leverage the resonance generated by the shunt and the capacitance of the piezoelectric transducer to passively establish a bandgap. However, such a configuration limits the flexibility of the bandgap's target frequency. For this reason, in this report, active piezoelectric metamaterials are analysed, consisting of a collocated sensor-actuator pair and a controller that closes the loop between the two in each unit cell. Such an active configuration allows for greater flexibility in terms of controller design and the bandgap's target frequency. This makes it a promising solution for reducing the transmission of both resonant and non-resonant disturbances.

This thesis will therefore focus on the use of elastic piezoelectric metamaterials in a sensor-actuator configuration for bandgap generation. The main application of this study concerns beam-like structures, which represent many typical precision systems like wafer grippers, leaf springs, or flexible manipulators. Given the motivation and relevance of the study presented thus far, the following section more clearly outlines the direction and objectives of the presented thesis. A dedicated section is intentionally included to demonstrate the decision-making process involved in selecting these.

1.2 Research Direction and Objectives

Although the sensor-actuator configuration of piezoelectric metamaterials was previously observed within the literature [10], no study was presented that applied this concept to generate local bandgaps in mechatronic applications. Hence, the original research direction was to experimentally implement such metamaterial architecture in beam-like structures to demonstrate their potential regulated use as a vibration isolation tool for the mechatronic industry. To this aim, an experimental comparison of different control approaches would also be conducted, in an attempt to improve the bandgap-generation performance of the outlined metastructure.

However, it was soon realised that the use of such a configuration involves parasitic effects that can limit the bandgap generation performance. Moreover, most of the research conducted in the literature primarily focuses on simulations, theoretical analysis, or experiments with extensive sampling times [11] [12], thereby overlooking the impact of such parasitic dynamics on the bandgap generation capabilities of these metamaterial architectures. A different question therefore arose: Do the bandgap-generation properties of such active piezoelectric metastructures remain adequate in the presence of parasitic effects for practical implementation in precision mechanisms?

In answering this question, the direction and objectives of the research shifted in an attempt to more significantly contribute to the existing literature. In particular, the main objective of the thesis is to investigate the practical issues involved in the experimental implementation of active piezoelectric metamaterials for both resonant and non-resonant vibration suppression. To fulfil this goal, a study is conducted to explore the effect of parasitic dynamics, such as time delay and RC roll-off characteristics of piezoelectric transducers, on both controller selection and system performance. Specifically, three commonly used controllers: Positive-Position Feedback (PPF) [13] [14], Negative-Position Feedback (NPF) [15], and Band-Pass Filter (BPF) control [16] are studied and their performance is compared. Moreover, analyses are presented first on a simplified system with a single mode, and subsequently on a full model using SPACAR. Ultimately, the modelled metamaterial architecture consisting of 7 unit cells is built and experimentally tested in a lab environment.

The following section explains the way the report is structured such as to successfully fulfill the outlined objective of the thesis.

1.3 Thesis outline

This thesis report is structured as follows:

- Chapter 2 introduces the fundamentals of metamaterial architectures, local resonance, the piezoelectric effect, and piezoelectric transducers. Additionally, the chapter outlines the different controllers compared. Note that this chapter was part of the literature survey report conducted for the thesis.
- Chapter 3 represents the main contribution of the thesis. Here, the objective of the thesis is fulfilled. This chapter is written in a paper format to be self-contained. Hence, some repetition of the information provided in the previous chapters occurs.
- Chapter 4 provides additional insights into the main contribution of the thesis. Specifically, this chapter reports the first steps conducted in an attempt to compensate for the parasitic dynamics of the experimental setup by implementing charge amplifiers.
- Chapter 5 offers concluding remarks on the thesis and provides recommendations for future work.
- Lastly, the included appendices elaborate on the experimental setup and components used (Appendix A), the practical work required to build it (Appendix B), the software code used (Appendix C), and the identified MIMO transfer function of the experimental setup (Appendix D). These sections serve as additional information explaining the process undergone to fulfil the objective of the study.

Chapter 2

Literature background

2.1 Metamaterials

For engineering structures and systems, especially within the high-tech precision industry, critical components and sensitive equipment need to be protected from excessive vibrations. For this purpose, research is growing in developing techniques for creating bandgaps. As mentioned briefly in Section 1.1, a bandgap is defined as a region in the frequency response of a system where the transmission of vibrations will approach zero. Within the literature, different domains can use different terms to express bandgap-like behaviours, such as roll-off, zeros of a system, or anti-resonance. However, the aforementioned terms are related and can be seen as synonyms in most cases.

Originally, the term bandgap was introduced in the field of applied physics in relation to electromagnetic waves [17]. Specifically, bandgaps were attained through the concept of Bragg scattering using photonic crystals, i.e., composites with periodically varying material properties [18]. Here, photonic crystals with photonic bandgaps were designed, preventing light from propagating in certain directions with specified frequencies. Bragg scattering occurs when the distance between the added structures equals half of the wavelength of the propagation wave. Hence, at frequencies where the Bragg condition is met, a gap opens where no waves can propagate. However, scattering-based bandgaps can only occur at wavelengths comparable to the lattice size of the material. Hence, in order to achieve stop bands in the low-frequency range, photonic crystals must be large, leading to bulky constructions which are unfeasible for many real-world applications. This is particularly inconvenient for vibration attenuation of elastic waves in lightweight and flexible structures, such as the blade-like systems present within the high-tech industry.

To bypass the limitations of photonic crystals, developments in the field of elastic metamaterials grew. Elastic metamaterials are systems with a small-scale repeated structure (called a unit cell) that yield large-scale effective properties that are not found in nature. Regarding vibration isolation, metamaterials are of interest because they allow for the creation of vibrational bandgaps at wavelengths much larger than their characteristic unit cell size, unlike photonic crystals. The concept of metamaterials is not unique to structural dynamics but is also widely researched in the fields of optics [19], acoustics [20], and heat transfer [21]. Liu et al. [22] were the first to experimentally demonstrate bandgaps at wavelengths much larger than the lattice size for elastic metamaterials.

2.1.1 Locally resonant metamaterials

The fundamental operating principle behind elastic (or resonant) metamaterials' bandgaps relies on local (active or passive) resonators (e.g., tuned mass dampers) in the unit cells, hence the name locally resonant metamaterials. In fact, at the natural frequency of the resonators, the majority of the vibrational energy is absorbed by the resonators themselves, implying they will displace the most, thus allowing for only a small portion of the energy to be transmitted to the structure and for a vibration attenuation region to be generated.

To easily and accurately identify the vibration attenuation (i.e., stopband) region, a dispersion diagram is used. Dispersion diagrams provide a relation between frequency ω and wave number k (also known as wave constant). Fig. 2.1 shows an example of a dispersion diagram. Here, the coupling of the local resonance (i.e., blue dotted line) to the wave (i.e., solid black line) leads to the opening of a bandgap at the corner frequency ω_0 of the local resonator. In particular, the coupling will split the degenerate system of the wave and the local resonator, with this effect being the strongest where the two frequencies cross. Hence, a frequency window where no wave can propagate will originate. To better understand this working principle, the idea of a local resonator (vibration energy absorber) such as a tuned mass damper (TMD) is explained.

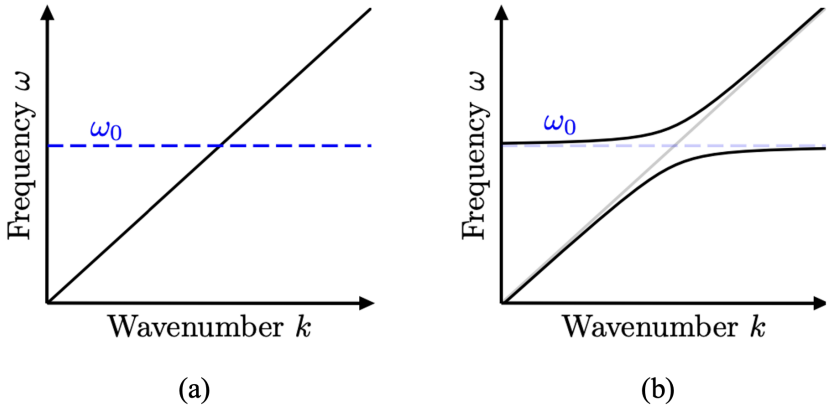

Figure 2.1: A dispersion diagram: (a) wave dispersion (black solid) and location of a local resonance (dashed blue); (b) coupling of the local resonance to the wave leading to the formation of a bandgap at ω_0. Adapted from [23].

A TMD (or vibration absorber) can be represented in its simplest mechanical form as in Fig. 2.2, consisting of a mass M_1, spring K_1, and damper C_1. It is mounted on a specific location in a structure of mass M_2, stiffness K_2, and damping C_2, so as to reduce the transmission of vibrations in the structure for a certain frequency range. In fact, at the corner frequency of the TMD: $\omega_{tmd} = \sqrt{\frac{K_1}{M_1}}$, a vibration attenuation region is generated within the structure, recall Fig. 2.1. The reason for this can be simply explained by looking at the transfer function between process disturbance d and the output of the system y,

$$\frac{y}{d} = \frac{G}{1 + GC} \tag{2.1}$$

where G is the plant system, and C is the tuned mass damper system acting as a controller. If

the local resonator C has no damping (i.e., $C_1 = 0$), but consists of a mass and spring only, then its resonance peak will go to infinity. When substituting this infinite C value in Eq. 2.1, then the transmissibility of the system will tend to $\frac{1}{\infty} = 0$ at the corner frequency of the resonator, providing ideal vibration isolation. For practical implementations, however, damping cannot be ignored and has to be considered, meaning that the resonance peak of C will have a finite value, thus resulting in a lower vibration attenuation within the system (i.e., $\frac{y}{d}$ is not exactly zero).

Hence, the parameters of the tuned-mass damper can be adjusted accordingly for a bandgap to be generated at a certain target frequency. Specifically, in order for a bandgap to be generated at low frequencies, as often desired in mechatronic applications, either the stiffness K_1 can be reduced or the mass M_1 of the TMD can be increased. However, because increasing the total mass of a system is undesired (especially in precision mechanisms), it is often the stiffness of the TMD that is reduced. More information on low stiffness mechanisms can be found in Section 2.2.1.

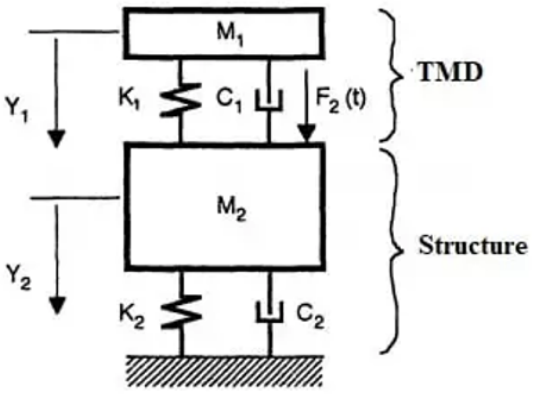

Figure 2.2: Schematic diagram of a TMD system, adapted from [24].

Therefore, in its mechanical form, a locally resonant metastructure consists of resonators in the form of tuned mass dampers within each unit cell, which allow for the generation of a bandgap in the frequency response of the system. An example of a mechanical locally resonant metastructure consisting of seven identical unit cells is illustrated in Fig. 2.3. The seven tuned mass dampers, one for each unit cell, are clearly visualised on the metastructure. In particular, the frequency at which the bandgap is generated corresponds to the tuned natural frequency of the resonators, based on the working principle of TMDs and the dispersion diagram previously explained in Fig. 2.1. Moreover, it is important to note that, in basic metamaterials, the corner frequencies of the local resonators within the unit cells are identical. Hence, the larger the number of unit cells (i.e., local resonators) within a metamaterial, the larger the vibration attenuation effects in the structure.

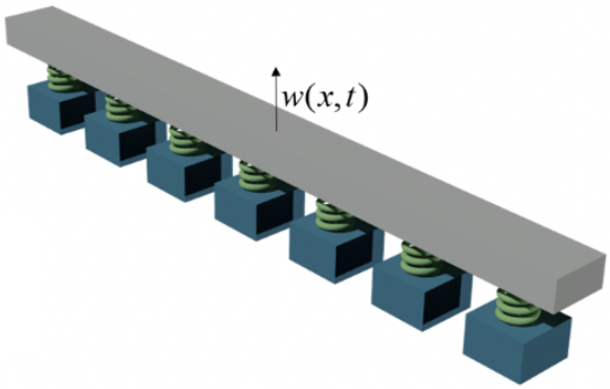

Figure 2.3: Example of a mechanical locally resonant metastructure with identical tuned-mass dampers in each unit cell for a beam undergoing transverse vibrations. Adapted from [25].

In the literature, locally resonant metamaterials are categorised into two different groups, depending on the resonator technique used: mechanical or electromechanical (also known as piezoelectric-based) metamaterials. In the former, resonators are often passive elements [26] such as tuned mass dampers (as in Fig. 2.3), whereas in the latter resonators are produced electronically using piezoelectric transducers. In this thesis, only piezoelectric-based metamaterials will be analysed and used. Hence, in order to properly understand their operating principles, a short introduction on piezoelectric transducers and how they are used for generating metastructures is provided in the following subsection.

2.1.2 Piezoelectric transducers in metamaterials

Piezoelectric transducers are commonly used in the field of Active Vibration Control [27]. The main advantages of these transducers include [28]: high power density, fast response, large force, high sensitivity, small hysteresis, and stability. Piezoelectric transducers can be applied in either actuation mode or sensing mode [29]. However, in order to properly understand the working principles of this type of transducer, the piezoelectric phenomenon needs to be explained first.

A piezoelectric material is one that produces electrical charges when mechanical stress is applied to it. This is also known as the direct piezoelectric effect, and is used in the sensing mode of the transducer. Besides this, the opposite is also possible, in that electrical charges can be provided to the piezoelectric material, which will in turn generate mechanical deformations. This is also known as the converse piezoelectric effect, and is used in the actuation mode of the transducer. In fact, piezoelectric materials are a special class of materials that, subject to an external electric field, can extend or contract depending on the internal polarization of the transducer and the orientation of the applied field. A schematic overview of this is illustrated in Fig. 2.4.

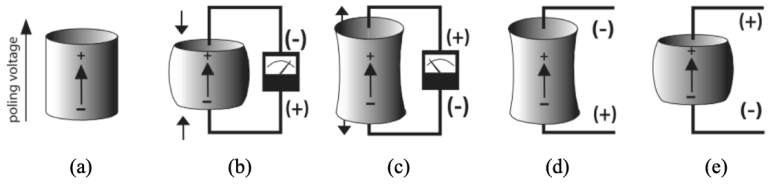

Figure 2.4: The piezoelectric effect [30]: (a) The poling direction; (b) Voltage generated in the poling direction due to compression; (c) Voltage generated in opposite direction of the poling direction due to tension; (d) Extension due to voltage in the poling direction; (e) Compression due to voltage in opposite poling direction.

The constitutive equations for a piezoelectric transducer in strain-charge format are obtained according to the IEEE standard on piezoelectricity. In particular, the equation for the converse piezoelectric effect, used in actuation mode, is as follows.

$$S_{ij} = s^E_{ijkl} T_{kl} + d_{kij} E_k \tag{2.2}$$

On the contrary, the equation for the direct piezoelectric effect, used in sensing mode, is shown below.

$$D_i = d_{ikl} T_{kl} + \epsilon^T_{ik} E_k \tag{2.3}$$

The constitutive equations describe the physical behaviour of a piezoelectric transducer, where the variables presented in Eqs. (2.2) and (2.3) are listed as follows with corresponding units and dimensions.

- S_{ij} is the dimensionless, [6 x 1] strain vector;
- T_{kl} in Pascals [Pa], is the [6 x 1] externally applied stress vector;
- E_k in [V/m], is the [3 x 1] electric field vector;
- D_i in [C/m^2] is the [3 x 1] electric displacement vector;
- s^E_{ijkl} in [m^2/N] is the [6 x 6] specific compliance matrix at constant electric field;
- d_{ikl} in [m/V] or [C/N] is the [3 x 6] piezoelectric coefficient matrix; and
- ϵ^T_{ik} in [F/m] is the [3 x 3] dielectric coefficient matrix at constant stress;

Note that the superscripts ^{E} and ^{T} indicate properties measured with a constant electric field and stress, respectively. Moreover, note that stress T_{kl} and strain S_{ij} tensor notations are often replaced by engineering vector notations for simplicity. Hence, in explicit forms, Eqs. (2.2) and (2.3) can be re-written as in Eqs. (2.4) and (2.5), respectively.

$$\begin{bmatrix} S_{11} \\ S_{22} \\ S_{33} \\ 2S_{23} \\ 2S_{31} \\ 2S_{12} \end{bmatrix} = \begin{bmatrix} s_{11} & s_{12} & s_{13} & 0 & 0 & 0 \\ s_{12} & s_{22} & s_{23} & 0 & 0 & 0 \\ s_{13} & s_{23} & s_{33} & 0 & 0 & 0 \\ 0 & 0 & 0 & s_{44} & 0 & 0 \\ 0 & 0 & 0 & 0 & s_{55} & 0 \\ 0 & 0 & 0 & 0 & 0 & s_{66} \end{bmatrix} \begin{bmatrix} T_{11} \\ T_{22} \\ T_{33} \\ T_{23} \\ T_{31} \\ T_{12} \end{bmatrix} + \begin{bmatrix} 0 & 0 & d_{31} \\ 0 & 0 & d_{32} \\ 0 & 0 & d_{33} \\ 0 & d_{24} & 0 \\ d_{15} & 0 & 0 \\ 0 & 0 & 0 \end{bmatrix} \begin{bmatrix} E_1 \\ E_2 \\ E_3 \end{bmatrix} \tag{2.4}$$

$$\begin{bmatrix} D_1 \\ D_2 \\ D_3 \end{bmatrix} = \begin{bmatrix} 0 & 0 & 0 & 0 & d_{15} & 0 \\ 0 & 0 & 0 & d_{24} & 0 & 0 \\ d_{31} & d_{32} & d_{33} & 0 & 0 & 0 \end{bmatrix} \begin{bmatrix} T_{11} \\ T_{22} \\ T_{33} \\ T_{23} \\ T_{31} \\ T_{12} \end{bmatrix} + \begin{bmatrix} \epsilon_{11} & 0 & 0 \\ 0 & \epsilon_{22} & 0 \\ 0 & 0 & \epsilon_{33} \end{bmatrix} \begin{bmatrix} E_1 \\ E_2 \\ E_3 \end{bmatrix} \tag{2.5}$$

In the literature, the terms of the piezoelectric coefficient matrix are given with the notation d_{ij}, where i indicates the direction of the electric displacement or field, and j indicates the direction of the mechanical strain or stress according to the designated directions shown in Fig. 2.5. Hence, different components of this matrix become relevant depending on the type of piezoelectric actuation. For instance, the coefficient d_{33} indicates that the strain and electric field are parallel to the poling direction. This is referred to as the piezoelectric gain for stack actuators, shown in Fig. 2.6(a). Similarly, d_{15} indicates that when the electric field is applied normally to the polarization direction, shear deformation occurs, resulting in the piezoelectric gain for shear actuators, shown in Fig. 2.6(b).

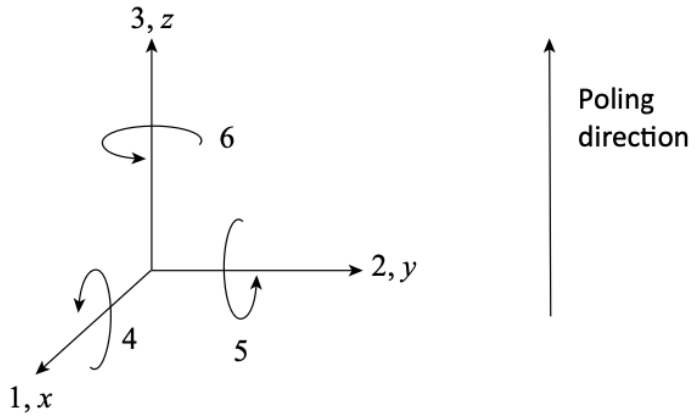

Figure 2.5: Piezoelectric coordinates related to the poling direction. Adapted from [31].

Different types of piezoelectric actuators exist, some of which have just been mentioned. However, the most relevant type of piezoelectric actuator for this study, employed in piezoelectric-based metamaterial structures, is illustrated in Fig. 2.6(c): the piezoelectric bending (or extension) actuator. This is also one of the most commonly used types of actuators in the field of AVC for flexible systems. Here, the actuators are bonded to the structure that needs to be controlled, and

rely on the d_{31} coupling coefficient. Hence, the actuators elongate (or shrink) in the longitudinal direction (i.e., direction 1) when an external voltage is applied along the poling direction (i.e., direction 3). Because the piezoelectric actuator is bonded to the system, its extension will result in a strain distribution in the structure, which ultimately induces bending, hence its name.

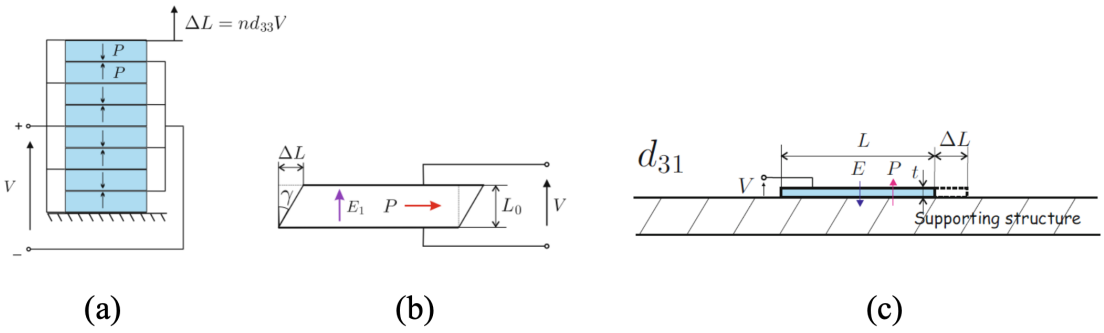

Figure 2.6: Different piezoelectric actuators: (a) piezoelectric stack actuator; (b) piezoelectric shear actuator; (c) piezoelectric bending actuator. Adapted from [1].

Typically, piezoelectric bending actuators are used in pairs, forming a system consisting of two active (piezoelectric) layers. Optionally, they can also have a passive layer (i.e., a central non-piezoelectric slab) between the two active layers. This way, when one patch elongates, the other shrinks, and the structure they are bonded to is subjected to a pure torque. Piezoelectric extension actuators used in pairs are defined as bimorph actuators, whereas they are defined as unimorph actuators when used individually; consisting of one active layer and one passive layer.

Therefore, a piezoelectric bimorph beam is obtained by symmetrically locating piezoelectric layers (or patches) sandwiching a central structural beam layer. Moreover, a metastructure is generated when the bimorph beam consists of N repeated piezo-patches along its length, where each paired piezoelectric layer represents one unit cell of the metamaterial. A visual representation of such a system is illustrated in Fig. 2.7. The analogy with its mechanical counterpart in Fig. 2.3 is evident. Here, all the piezoelectric patches are poled in the thickness direction, and the inner electrodes are combined through a conductive substrate, which yields a parallel connection under transverse vibrations. This thesis will focus on analysing the metamaterial bandgaps of horizontal bimorph beam structures only. There are three main reasons for this: (1) piezoelectric transducers are commonly used in mechatronics and AVC applications due to their numerous advantages, previously outlined at the beginning of this section; (2) piezoelectric patches have a smaller impact on a system's total mass compared to TMDs, which is desired in precision mechanisms; (3) such systems are analogous to the typical beam-like structures found in the mechatronic industry, which represent the main application domain of this study.

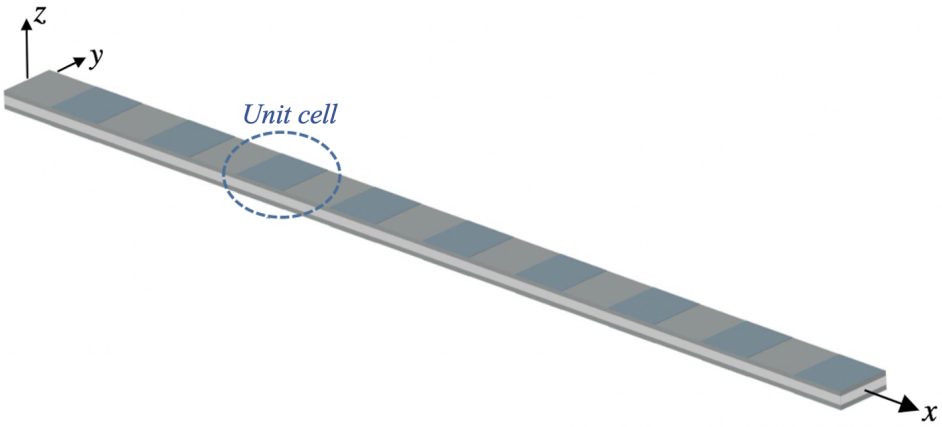

Figure 2.7: Example of a piezoelectric-based locally resonant metastructure with bimorph piezoelectric patches in each unit cell for a beam undergoing transverse vibrations. Adapted from [32].

As previously outlined, locally resonant metamaterials generate bandgaps based on the local resonance principle, where resonators are within each unit cell of the metastructure. Therefore, for a piezoelectric-based metamaterial such as the one shown in Fig. 2.7, the bimorph piezoelectric transducers of each unit cell (again, labelled within the image) can be used as resonators for generating bandgaps in three different ways:

1. **Passive:** This can be achieved through resonant shunting, which consists in connecting electronic components to the electrodes of the transducers bonded to the beam [33]. In particular, the added electric components will be the electrical analogues of a tuned mass damper (i.e., a dynamic vibration absorber). This way, the circuit dissipates the energy by making use of the resonance created by the shunt and the capacitance of the piezoelectric transducer. Hence, significant vibration attenuation is attained.

2. **Semi-active (or semi-passive):** Here, the passive shunt circuits in (1) are supplemented by the use of digital circuits such as operational amplifiers. Hence, the circuit requires an external energy source but does not deliver it to the structure for vibration suppression, as the vibration attenuation is passively provided by the shunt circuit, thus the name semi-active (or semi-passive).

3. **Active:** External energy sources are directly applied to the actuating piezoelectric patches in order to suppress the vibrations in the structure. Such a configuration will require a sensor to measure the system's vibrations, as well as a controller in-between the sensor and the actuator. In the control system, the sensor will provide the input signal, and the actuator will receive the output signal. Dealing with piezoelectric transducers, such a structure is easily attained by setting the patches on one side of the bimorph beam in actuation mode, and those on the other side in sensing mode.

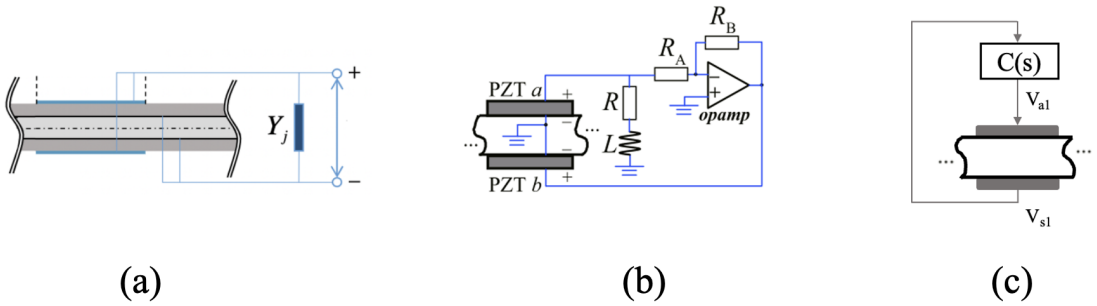

Figure 2.8: Resonating techniques in bimorph beams: (a) passive, adapted from [32]; (b) semi-active (or semi-passive), adapted from [34]; (c) active.

The above-listed resonating techniques used in bimorph beams are also represented visually in Fig. 2.8. For this thesis, only active vibration control techniques will be used, as they allow for more freedom in terms of their design and implementation. The detailed system architecture and the control algorithms used are discussed in greater depth in the following section.

2.1.3 Active control in metamaterials

Active control for generating locally resonant bandgaps in bimorph beam metastructures such as the one in Fig. 2.7 require three main components, which are: (1) a sensor to measure vibrations in the system, where in this case the piezoelectric sensor is placed on the host structure itself; (2) an actuator to directly control and suppress the vibration in the structure; and (3) a control system that closes the loop between the sensor, which is the controller input, and the actuator, which will receive the output signal of the controller. In this thesis, the piezoelectric transducers on the bottom part of the beam are in sensing mode, whereas those on the upper part of the beam are in actuation mode. Hence, within each unit cell of the metastructure, an individual control loop is formed, which acts as a local resonator.

Such a control architecture is also known as a decentralised control strategy. In fact, bimorph metastructures are often considered decentralised systems. Here, the data measured by each sensor is not combined, but individually employed in an independent control sub-system. A schematic representation of the decentralised control strategy adopted in a piezoelectric-based beam metastructure such as the one previously presented in Fig. 2.7 is illustrated in Fig. 2.9. In this figure, the metastructure consists of four unit cells, hence variables will have a subscript i where $i = 1, 2, 3, 4$ defines the unit cell considered. In the presence of mechanical vibrations, the bimorph beam will displace, and all the piezo-sensors at the bottom of the metastructure will produce an electric voltage V_{si}. These voltage signals will feed into controllers, $C(s)$, which will output a voltage signal V_{ai} for the piezo-actuators at the top of the structure. In a decentralised system, robustness and reliability are increased, as the computations for the individual unit cells can be performed in parallel. Moreover, the computational efficiency is high, thanks to distributed computing in real-time [35].

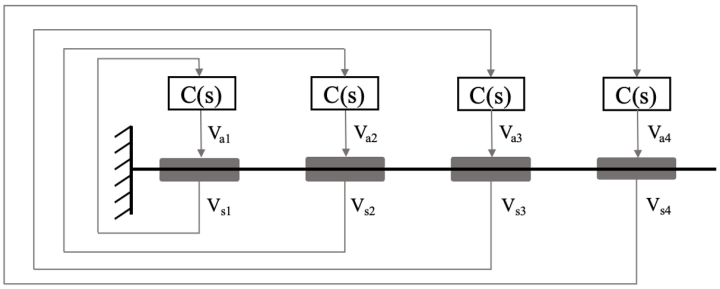

Figure 2.9: Schematic representation of the decentralised control strategy used in a bimorph beam metastructure consisting of four unit cells.

Given such a control architecture, in order for the unit cells to be locally resonant, the control algorithms employed within the controller blocks $C(s)$ of Fig. 2.9 are important. Based on the knowledge obtained in Section 2.1.1, where mechanical resonators in the form of tuned mass dampers were implemented within each unit cell of the metastructure to generate bandgaps, an electrical equivalent can be achieved within the controllers. From the literature, this corresponds to an NPF controller. This is introduced and more clearly outlined in Section 2.2.4. By implementing such transfer function as a controller $C(s)$ within the unit cells of the metamaterial, a locally resonant bandgap can be obtained. It is important to note that the controllers $C(s)$ do not vary from cell to cell, but rather remain unchanged throughout the metamaterial, just as with its mechanical counterpart in Fig. 2.3. In fact, there, all unit cells consisted of the same tuned mass damper, as explained.

Such metastructures are also known as piezoelectric-based metamaterials, and represent the electrical analogue of mechanical metamaterials such as the one introduced in Fig. 2.3. The former exploits piezoelectric transducers and a decentralised control architecture to generate bandgaps without adding any mechanical elements such as TMDs to the base structure. This has numerous advantages for applications within the precision industry, as briefly mentioned earlier in this section. Firstly, nowadays, piezoelectric transducers are commonly used within the industry due to their numerous benefits, hence making their application for generating locally resonant metastructures more straightforward compared to implementing mechanical resonators. Secondly, for generating metastructures in beam-like systems, piezoelectric transducers allow for a significantly low deviation in terms of mass, mode shapes, and resonant frequencies of the host structure. This is particularly useful for modern mechatronic applications, where systems are becoming increasingly lightweight and adding mass is not ideal.

However, it is important to note that the literature conducted thus far regarding locally resonant elastic metamaterials (i.e., both mechanical and piezoelectric-based) was based on studies from the field in the area of applied physics, which uses the infinite-resonators assumption. What this means is that the predicted vibration isolation performance of dispersion diagrams (Fig. 2.1) can only be attained if the metamaterial consists of an infinite number of unit cells. This way, the locally resonant bandgap edge frequencies are derived in closed form, and the infinitely long metastructure can be described by analysing a single cell. However, this infinite-resonators approximation is obviously not practical for physical realisations of metamaterials and, therefore, obtaining the expected performance in finite blade-like systems is virtually impossible. Nonetheless, in an attempt to push for the physical realisation of metastructures, research grew in studying the performance of metamaterials consisting of a finite number of resonators. Further investigations are outlined in the following section, Section 2.1.4.

2.1.4 Finite metamaterials

Based on the insights obtained regarding locally resonant metastructures in Section 2.1.1, it is clear that the vibration attenuation efficacy can be improved by increasing the number of local resonators (i.e., unit cells) N within the structure. In fact, the performance predicted by dispersion diagrams is exact only as $N \to \infty$. For practical design purposes and implementations, it is therefore important to investigate whether the dispersion diagram predictions can be used for cases of finite N.

By considering a uniform cantilever beam of length L with N equally spaced resonators, the effect of N on the nature of a metamaterial's bandgap formation was investigated in [36], and the performance compared to the predictions made by dispersion diagrams when $N = \infty$. Firstly, it was found that a certain minimum number of attachments (i.e., unit cells) are necessary for the formation of a bandgap. Secondly, and most importantly, it was found that the bandgap width predicted by dispersion diagrams (Fig. 2.1) $\Delta\omega_\infty$ is generally not the maximum attainable width $\Delta\omega(N)$. Therefore, this means that there exists a finite, optimal value N_{opt} which maximises $\Delta\omega(N)$ for a particular structure. Fig. 2.10 shows the variation in a metamaterial's bandgap width $\Delta\omega(N)$ as a function of the number of resonators N (or unit cells) in the structure, where ω_t is the target frequency for the bandgap generation. Here, an optimal value N_{opt} is clearly visualised, yielding better performance than that predicted using dispersion diagrams, which is promising for the practical implementations of metastructures in physical systems, including blade-like structures in mechatronics. Moreover, the poor performance of metamaterials for a low number of unit cells ($N < 3$) is confirmed, and the convergence towards $\Delta\omega_\infty$, based on the infinite-resonators assumption, is also observed as $N > 6$. It is important to note that the optimal number of unit cells, N_{opt}, will differ depending on the type of structure considered and the target frequency ω_t.

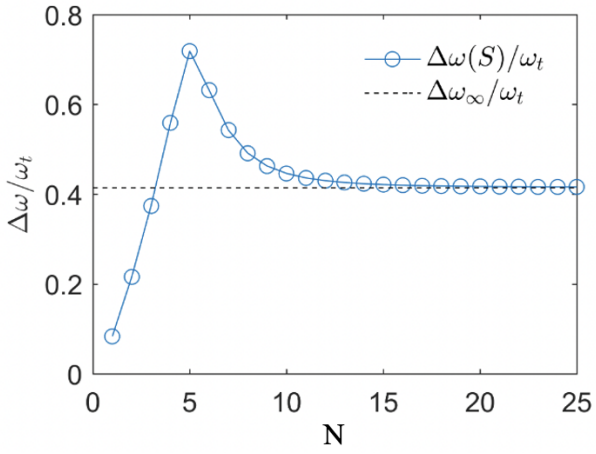

Figure 2.10: Effective bandgap width versus number of resonators N for a cantilever beam. Maximum bandgap width given at $N_{opt} = 5$. Adapted from [36].

The existence of a finite, optimal number of resonators N_{opt} suggests that there are some inefficiencies in placing a large number of resonators across the entirety of a structure. It is known that the energy stored by a particular resonator is related to its displacement which, in turn, is related to the host structure's displacement at the location of the unit cell. Hence, when multiple

resonators are placed evenly on a structure, some will move less than others, ultimately reducing the total amount of energy stored. Therefore, using a limited, finite number of resonators can reduce the inefficiencies within the metastructure and eventually increase the frequency range at which the unit cells store energy - i.e., increase the width of the generated bandgap, as shown in Fig. 2.10.

The relevance of this section is mainly aimed towards proving that, although metamaterials are researched based on the infinite-resonator approximation in the literature, they can nonetheless still be applied in finite physical systems with the same if not better vibration isolation properties. In the context of mechatronics, the larger bandgap produced by using N_{opt} is beneficial. However, the analysis necessary for obtaining N_{opt} in an arbitrary structure is cumbersome, and thus the study shown in Fig. 2.10 is more useful for proving the effectiveness of metamaterials in finite systems, rather than for actually improving the bandgap regions generated.

2.2 Vibration attenuation methods

2.2.1 Vibration isolation in the mechatronic industry

Vibration isolators such as tuned mass dampers, previously presented in Section 2.1.1 (Fig. 2.2), are extensively studied in the literature. Thus, in theory, it is known that for vibration isolation at low frequencies, as desired in precision mechanisms, the elastic stiffness of the isolator should be made as small as possible. However, in practice, care needs to be taken in that if the stiffness is too small, large static displacements will arise in the system, which are detrimental especially in the high-tech industry. The trade-off between isolation and static displacement is therefore critical. To overcome such a trade-off, quasi-zero stiffness (QZS) mechanisms have been studied and developed in the literature [37] [38]. These are obtained by careful choice of the system parameters, by combining negative stiffness elements (e.g., oblique springs) with positive ones. The outcome is thus an isolator with quasi-zero dynamic stiffness at the static equilibrium position, which enables low transmissibility for a broad frequency range without causing the detrimental effects mentioned. Typical applications of QZS mechanisms include the isolation of high-precision machinery, and thus relevant for this study.

However, passive vibration isolation methods such as QZS systems or TMDs are often not sufficient, on their own, for effective vibration attenuation in mechatronic high-precision mechanisms. This is particularly true when considering the increasingly strict demands that need to be satisfied within the high-tech industry, such as high bandwidths and broadband low-frequency vibration isolation. For this reason, in recent years, the combination of passive vibration isolators with active control methods such as feedforward has become increasingly dominant [39]. A disturbance feedforward controller consists of a filter that is placed in series with the plant in order to compensate for its dynamics [31]. Typically, the controller inputs are measurements from external disturbances (such as floor vibrations), used to compute the control action. The idea is that a feedforward signal is computed in advance and acts against the disturbance to be compensated. The main advantage of feedforward control is achieving an increase in vibration attenuation performance without necessarily affecting the closed-loop stability properties of the system. For applications in the high-tech industry, feedforward controllers are in the form of self-tuning filters [40].

Still, feedforward control has its own limitations. Specifically, feedforward control requires an accurate dynamic model of the transfer function from base vibrations to system vibrations, which is often difficult to obtain from modelling and identification experiments. Hence, the

estimated model parameters for feedforward control are never known exactly, and the maximum achievable performance is limited by the error term. Striving for maximum predictability of the dynamic behaviour of a mechatronic system is a pivotal part of the design, thus making feedforward control further impractical. Moreover, feedforward control is typically undesired for the suppression of low-frequency disturbances, as this often leads to drift and actuator saturation [41]. The inevitable residual errors of feedforward control are often corrected by feedback control. For this reason, feedback control is often preferred to achieve small steady-state errors, either in combination with feedforward control or without.

Feedback control is naturally more complex and critical to design compared to feedforward control, mainly due to the risk of instability. Within the high-tech industry, motion systems with inherent instability, which exhibit poles in the right-half-plane, such as magnetic bearings, or free-floating objects, require feedback control for stabilisation. Active control in the context of feedback control has typically meant active damping control [42] [15], which aims to reduce the resonant vibrations of a system, and goes beyond the scope of this study. However, a novel feedback technique for narrowband control of non-resonant vibrations was introduced in 2016 by Kim *et al.* [16]. This was shown to provide promising results for bandgap generation in systems, and is outlined in greater detail in the following subsection, 2.2.2.

2.2.2 Narrowband feedback control

The main focus of the study in [16] was to investigate narrowband position and acceleration feedback for out-of-resonance vibration control. Experiments demonstrated that the two methods are related to active stiffness for bandgaps at frequencies well below resonance, and inertial control for bandgaps at frequencies well above resonance, respectively. The control approach was validated on a single-degree-of-freedom system consisting of mass m_s, spring k_s, and damper c_s, with respective corner frequency $\omega_s = \sqrt{k_s/m_s}$. For the controller implemented, the narrowband (negative) feedback control force was defined as,

$$f_c = -\left[kB_p(\omega)u + cB_v(\omega)\dot{u} + mB_a(\omega)\ddot{u}\right] \tag{2.6}$$

where u, $\dot{u}$, and $\ddot{u}$ represent the position, velocity, and acceleration of the system in the frequency domain, respectively, such that $\dot{u} = \ddot{u}/j\omega$, and $u = \ddot{u}/(j\omega)^2$. The three terms inside the brackets of Eq. (2.6) correspond to narrowband position, velocity, and acceleration feedback, consisting of the control gains k, c, and m, as well as the filters $B_p(\omega)$, $B_v(\omega)$, and $B_a(\omega)$, respectively. However, because narrowband velocity feedback (i.e., $cB_v(\omega)\dot{u}$) is a common way of realising an Electrical Dynamic Absorber (EDA) for resonant vibration control [3], this will not be further investigated. Each filter is a second-order bandpass filter,

$$B_i(\omega) = \frac{2\zeta_i\omega_i s}{s^2 + 2\zeta_i\omega_i s + \omega_i^2} \tag{2.7}$$

where $i = p$, and a for the position, and acceleration, respectively, ω_i represents the corner frequency of the controller, and ζ_i is the damping ratio. The main aim of the controller is for it to selectively extract and consequently feed back the targeted in-phase signal component only. Hence, the corner frequency of the controller ω_i should be tuned to a low frequency for position feedback (i.e., in the stiffness-controlled region, $\omega_p << \omega_s$), and high frequency for acceleration feedback (i.e., mass-controlled region, $\omega_a >> \omega_s$). The corresponding controllers for position ($C_p(j\omega)$) and acceleration ($C_a(j\omega)$) narrowband feedback are respectively as follows.

$$C_p(j\omega) = k \cdot B_p(\omega) \tag{2.8}$$
$$C_a(j\omega) = m \cdot B_a(\omega) \tag{2.9}$$

The controllers $mB_a(\omega)$ and $kB_p(\omega)$ act as added mass and spring to the system around the pass band of the filters, respectively. Thus, they may be called a narrowband electrical mass and spring.

According to the Nyquist robustness criterion, a control system is stable and robust with a degree l_0 if and only if its open-loop frequency response function (FRF) locus does not enclose or cross the circle of radius l_0 centred at the instability point (-1, 0). Hence, a robustness constraint can be formulated for a stable controller:

$$RR(dB) \leq 20 \log_{10} l_0^{-1}, \quad \forall\omega \tag{2.10}$$

where $RR(dB)$ represents the reduction ratio, in decibels, and $0 < l_0 < 1$. The limiting value on the right-hand side of Eq. (2.10) is the maximum allowable control spillover defined as $RR_{max} = 20 \log_{10} l_0^{-1}$. Since the maximum control spillover occurs at the plant's natural frequency ω_s, also the following constraint can be formulated for the controllers:

$$gb_i \leq 2\zeta_s \cdot \eta \cdot (1 - l_0) \tag{2.11}$$

where g is the normalised controller gain $g = k/k_s$ for position feedback, or $g = m/m_s$ for acceleration feedback, b_i is the controller bandwidth $b_i = b_p$ or $b_i = b_a$ for position and acceleration, respectively, and ζ_s is the damping in the considered structure. Moreover, $\eta = \omega_s/\omega_p$ or $\eta = \omega_a/\omega_s$ depending on the type of feedback controller used, and always $\eta > 1$. Hence, from Eq. (2.11) it is understood that, under a certain degree of robustness l_0, the control bandwidth (related to gb_i) can be improved if the structure is more highly damped (i.e., higher ζ_s), and/or if the corner frequency of the controller (either ω_p or ω_a) is further away from the plant natural frequency ω_s (i.e., higher η), suggesting that the controllers are more effective at very low frequency for position, and very high frequency for acceleration feedback. The low-frequency range is of particular interest for mechatronic systems, suggesting how narrowband position feedback can be used beneficially for the vibration isolation of high-tech mechanisms.

Experimental results on the single-degree-of-freedom system considered in [16] are illustrated in Fig. 2.11a for narrowband position feedback, and in Fig. 2.11b for narrowband acceleration feedback. In both cases, the spillover at the plant corner frequency ω_s can be observed. Moreover, it was demonstrated how narrowband position and acceleration control were effective in controlling the system's low-frequency and high-frequency non-resonant vibrations, respectively.

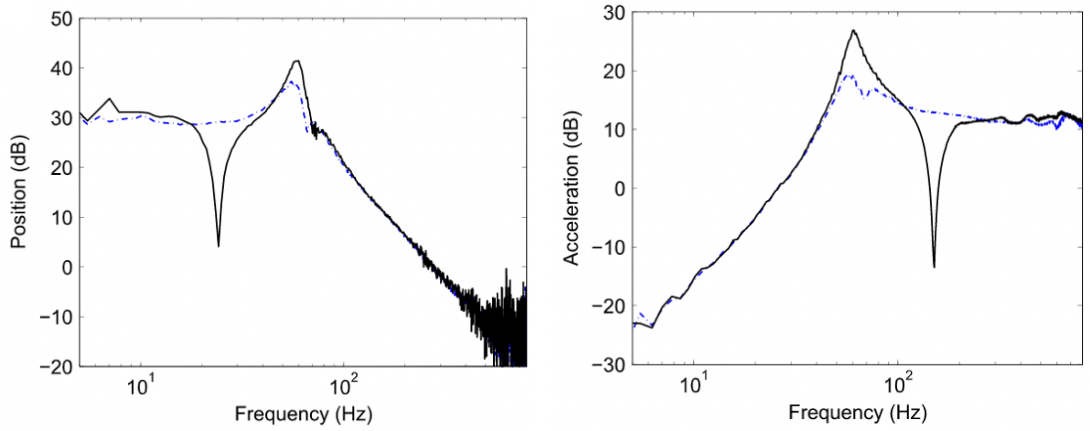

(a) (b)

Figure 2.11: Impact test results of a single-degree-of-freedom system before (blue dash-dot line) and after (black solid line) control for narrowband (a) position feedback; (b) acceleration feedback. Figures adapted from [16].

Indeed, given its impressive low-frequency vibration attenuation properties, the narrowband position (negative) feedback control approach presented in [16] and outlined so far can be implemented within metamaterial architectures for generating bandgaps. The following sections outline other similar feedback control strategies studied in the literature that can also be implemented within metamaterial architectures for generating bandgaps in beam-like mechatronic structures.

2.2.3 Positive Position Feedback control

Positive Position Feedback (PPF) was originally introduced by Fanson and Caughey [13]. Nowadays, it is extensively used within the literature for active damping of flexible structures integrating piezoelectric transducers [43]. A PPF controller uses position as the sensed signal, which is then positively fed back to the system through a second-order low-pass filter. This explains why PPF controllers are commonly used with piezoelectric transducers, as these sense position. The transfer function of a PPF controller is given as,

$$H(s) = -\frac{g}{s^2 + 2\zeta_f \omega_f s + \omega_f^2} \tag{2.12}$$

where ω_f is the controller's corner frequency, g the gain, and ζ_f the damping ratio. PPF can be implemented in parallel to dampen multiple vibration modes of a system by tuning each filter at one specific mode frequency. Such a configuration is shown in Fig. 2.12, where ω_{f1}, ω_{f2}, and ω_{f3} correspond to the first, second, and third modes of the plant $G(s)$, respectively. With such a configuration, all three resonant modes are damped.

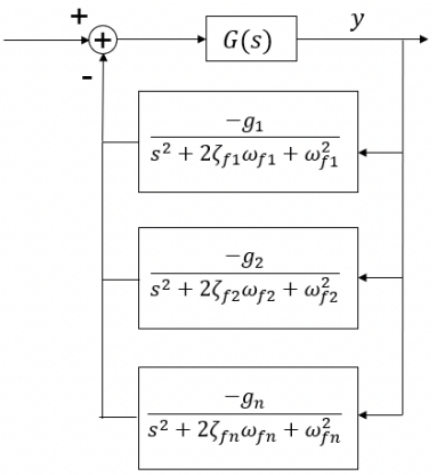

Figure 2.12: Closed-loop system with parallel PPF controllers.

The disadvantages of PPF control include low-frequency spillover, which can result in a change in resonance frequency. On the positive side, however, high-frequency spillover is prevented by the low-pass filter's roll-off at higher frequencies.

Typically, PPF controllers are used for active damping, as previously outlined, but the presence of a resonance peak at the filter's corner frequency allows for it to be implemented within a metamaterial architecture to generate a bandgap in the frequency domain. Hence, the bandgap generation performance of such a controller within a metamaterial architecture can also be analysed.

2.2.4 Negative Position Feedback control

Negative Position Feedback (NPF) control was initially introduced in [44] and discussed in [45]. Here, the controller uses position as the sensed signal, and then negatively feeds it back to the system through a second-order high-pass filter. When a generalised displacement sensor such as a piezoelectric transducer is used, the literature [46] shows how a NPF controller is the electrical realisation of a dynamic vibration absorber. This has a transfer function as,

$$H(s) = \frac{gs^2}{s^2 + 2\zeta_f \omega_f s + \omega_f^2} \tag{2.13}$$

In terms of limitations, the absence of roll-off at higher frequencies causes high-frequency spillover, especially when modes are closer together. Therefore, such an architecture is found to be optimal for high-frequency control, as this causes limited spillover in the lower-frequency region. This is not the case for PPF control. The combination of PPF and NPF control is also assessed in the literature [15]. As with PPF control, the resonant frequency of the high-pass filter allows for practical implementation within active piezoelectric metamaterial architectures.

Chapter 3

Metastructures in a sensor-actuator configuration: the practical issues in bandgap generation

Metastructures in a sensor-actuator configuration: the practical issues in bandgap generation

Francesco Coatto
Precision and Microsystems Engineering
Delft University of Technology
Delft, Netherlands
fcoatto@tudelft.nl

Marcin Kaczmarek
Precision and Microsystems Engineering
Delft University of Technology
Delft, Netherlands
M.B.Kaczmarek@tudelft.nl

Hassan HosseinNia
Precision and Microsystems Engineering
Delft University of Technology
Delft, Netherlands
S.H.HosseinNiaKani@tudelft.nl

***Abstract*—The emerging field of elastic (locally resonant) metamaterials offers a viable solution to suppress unwanted vibrations by generating bandgaps in both resonant and non-resonant regions. The main contribution of this paper consists in studying the practical issues involved in the experimental implementation of such metamaterial architectures, often overlooked in the literature. To this aim, parasitic dynamics such as time delay and RC roll-off characteristics of piezoelectric transducers are considered, and their influence on controller choice is evaluated. The latter was found to be significant in limiting the bandgap generation capabilities of the system in non-resonant regions. The reason for this was the added phase caused by the parasitic effect, which required a reduction in controller gain for stability and ultimately reduced the bandgap performance. This was not the case for resonant bandgaps, as the parasitic phase lead was compensated by the increase in gain at the resonance, ultimately allowing for optimal resonant bandgaps to be generated. The research was conducted using full model simulations in SPACAR and an experimental setup.**

***Index Terms*—Bandgap, locally resonant metamaterials, parasitic dynamics.**

I. Introduction

Undesired vibrations are one of the most significant sources of error in any type of mechatronic system or component. The detrimental effects of unwanted vibrations are particularly important in the precision industry, where these can significantly limit the performance of systems and in the worst cases cause failure [1]. Vibrations in mechatronic systems arise for a number of reasons. For instance, vibrations can be transmitted through direct forces acting on the base of a structure, such as the ground or a motion system. Alternatively, vibrations can be induced by transient excitations from nearby roads or human activities in the building. Therefore, it is necessary for solutions to be adopted for these vibrations to be successfully suppressed.

Metamaterials present a viable solution thanks to their ability to generate bandgaps, which are frequency ranges where the transmission of vibrations will approach zero. Metamaterials are specially engineered composites consisting of a small-scale repeated structure (called a unit-cell) that yields large-scale effective properties not found in nature. Examples include negative refractive index [2] or negative effective modulus [3]. Indeed, a possible application for metamaterials in precision mechanisms lies in their ability to generate bandgaps.

Specifically, the emerging field of elastic (locally resonant) metamaterials has proven to be promising in generating low-frequency bandgaps based on the exceptional results conferred in the area of applied physics [4]. Here, bandgaps can be attained by incorporating resonators such as passive tuned mass dampers in the unit cells that form the metamaterial. These allow for a greater degree of freedom thanks to the tuning of the resonator's natural frequency. In fact, at the resonator's corner frequency, most of the vibrational energy is absorbed internally, leaving only a limited amount to be transmitted to the structure. This absorption ultimately creates a vibration attenuation region, also known as a bandgap.

Liu et al. [5] were the first to experimentally demonstrate bandgaps at wavelengths much larger than the lattice size for elastic metamaterials. Since then, numerous papers have used locally resonant elastic metamaterials to generate bandgaps in structures, categorising them into two different groups: mechanical [6] and electromechanical (piezoelectric) [7] metamaterials. In the former, resonators such as mechanical TMDs are used, whereas in the latter resonators are electronically generated using piezoelectric transducers. In this paper, only piezoelectric metamaterials will be used. There are three main reasons for this: 1. piezoelectric transducers are commonly used in mechatronics and AVC applications due to their numerous advantages [8], hence making their implementation more straightforward; 2. piezoelectric transducers have a smaller impact on a system's mass, mode shapes, and resonant frequencies compared to mechanical resonators, which makes them more ideal for precision systems; and 3. such systems are analogous to the typical beam-like structures found in the precision mechatronic industry, hence making them well-suited for such applications.

In piezoelectric metamaterials, resonators in the form of shunt circuits are commonly implemented in the unit cells [9]. These circuits leverage the resonance generated by the shunt and the capacitance of the piezoelectric transducer to passively establish a bandgap. However, this configuration limits the design freedom of the bandgap's target frequency. For this reason, in this paper, active piezoelectric metamaterials are analysed, consisting of a collocated sensor-actuator pair and a controller that closes the loop between the two in each unit cell. Such configuration has already been used within

the literature [10], as it allows for more freedom in terms of controller design and ease of implementation. However, the use of such a configuration involves parasitic effects that can limit the bandgap generation performance. Moreover, most of the research conducted in the literature primarily focuses on simulations, theoretical analysis, or experiments with extensive sampling times [11] [12], thereby overlooking the impact of such parasitic effects, including the two most significant dynamics: time delay and the RC roll-off characteristic of piezoelectric transducers. The question thus is whether the bandgap-generation properties of such active piezoelectric metastructures remain adequate for practical implementation.

Therefore, the main contribution of this paper is to investigate the practical aspects involved in the implementation of such active bandgap-generating elastic metamaterials for both resonant and non-resonant vibration suppression. To achieve this, a study of the parasitic dynamics involved, as well as the influence these have on the controller choice and performance of the system is made. Specifically, three commonly used controllers: Positive-Position Feedback (PPF) [13], Negative-Position Feedback (NPF) [14], and Band-Pass Filter (BPF) control [15] are studied and their performance is compared. Analyses are first conducted on a simplified system with a single mode, and subsequently on a full model using SPACAR. Ultimately, the modelled metamaterial architecture consisting of eight unit cells is built and experimentally tested in a lab environment. The main application of this study concerns beam-like structures, which represent many typical precision systems like wafer grippers, leaf springs, or flexible manipulators.

This paper is structured as follows: in Section II, the structure of active piezoelectric metamaterials, their control architecture, and the simplified system model is introduced. In Section III, the simplified model is used to study the effect of parasitic dynamics when experimentally implementing such active piezoelectric metamaterials for resonant and non-resonant bandgaps. Section IV presents the results attained using the full SPACAR model of the experimental setup, which is in turn introduced in Section V together with the obtained experimental results. Lastly, the research is concluded in Section VI.

II. Active Piezoelectric Metamaterials Architecture

In this section, the structure of an active piezoelectric metamaterial beam and its simplified model is presented first. Then, an overview of the corresponding control architecture and the studied controllers is provided. Lastly, the ideal performance of the controllers is compared when implemented on the outlined simplified system model.

A. Active Piezoelectric Metamaterial Beam

One way to achieve active piezoelectric metamaterial structures is by positioning piezoelectric transducers on both sides of a central beam in a collocated manner. This configuration, known as a "bimorph" beam, forms a single unit cell of the metastructure. The complete metamaterial architecture is hence generated once the beam is covered with N repeated collocated piezoelectric transducers along its length. In this configuration, all the piezoelectric patches are poled in the thickness direction. A visual representation of such a structure with $N = 4$ unit cells is shown in Fig. 1. Here, $i = 1, 2, 3, 4$ defines the unit cell considered, V_{si} is the voltage produced by the i-th sensor, V_{ai} is the voltage sent to the i-th actuator, and $C_i(s)$ are the identical controllers for each unit cell i. Specifically, the patch sensor output is related to the average beam curvature at its location, whereas the actuator produces a pair of moments with amplitudes proportional to the applied voltage. In analysing the transmissibility of the system, the transfer function from transverse force excitations F_z at the base, to transverse displacement at the tip of the beam z_{tip} is of interest. This is because, in mechatronics, it is the transmissibility at the tip of beam-like systems that is important for vibration isolation, and thus will allow for the bandgap performance to be adequately analysed.

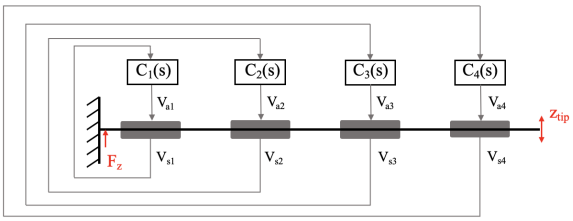

Fig. 1. Schematic representation of active piezoelectric metamaterials' architecture.

The dynamics from F_z to z_{tip} define the performance channel of the system. This is the transfer function where the bandgap is desired. The collocated channel, instead, is defined as the transfer function from actuator voltage V_{ai} to collocated sensor voltage V_{si}. Therefore, the desired outcome of such an architecture is that the dynamics imposed by the controllers $C_i(s)$ on the collocated channels generate a bandgap in the performance channel. In analysing the complex metamaterial structure presented in Fig. 1, a simplified system model is introduced first. This is truncated to have only one mode and consists of a beam with a single collocated sensor-actuator pair (i.e., a single unit cell). The equations of motion of such a system are

$$\begin{bmatrix} \ddot{x} \\ \dot{x} \end{bmatrix} = \begin{bmatrix} -2\zeta\omega_n & -\omega_n^2 \\ 1 & 0 \end{bmatrix} \begin{bmatrix} \dot{x} \\ x \end{bmatrix} + \begin{bmatrix} 1 & 1 \\ 0 & 0 \end{bmatrix} \begin{bmatrix} x_0 \\ V_a \end{bmatrix} \quad (1)$$

$$\begin{bmatrix} x \\ V_s \end{bmatrix} = \begin{bmatrix} 0 & 1 \\ 0 & 1 \end{bmatrix} \begin{bmatrix} \dot{x} \\ x \end{bmatrix} + \begin{bmatrix} 0 & 0 \\ 0 & 10 \end{bmatrix} \begin{bmatrix} x_0 \\ V_a \end{bmatrix} \quad (2)$$

where x, x_0 represent the tip and base displacements, ω_n is the system's resonant frequency, and ζ the modal damping of the structure. The controller's input V_s is related to a feedthrough term which is typical for collocated piezoelectric transducers [16]. Note that this simplified system will not be used to assess the performance of the different controllers in generating bandgaps, but rather to provide preliminary insights on the effects of parasitic dynamics on the closed-loop responses. For this reason, arbitrary system parameters were assigned, namely $\omega_n = 1$ rad/s and $\zeta = 1\%$.

B. Control Architecture

Active control for generating locally resonant bandgaps in beam-like piezoelectric metastructures such as the one in Fig. 1 require three main components: 1. a sensor to measure vibrations in the system; 2. an actuator to directly control and suppress the vibrations in the structure; and 3. a control system that closes the loop between the sensor and the actuator. Hence, within each unit cell of the metastructure, an individual control loop is formed, which acts as a local resonator. A decentralised control strategy is therefore adopted, where the data measured by each sensor is not combined, but individually employed in an independent control sub-system, increasing both robustness and reliability as computations for the individual unit cells can be performed in parallel [17]. Fig. 2 shows the closed-loop block diagram corresponding to the metamaterial structure presented in Fig. 1. Here, the controllers' $C_i(s)$ ultimate objective is to limit the influence of base excitations F_z on the tip displacement z_{tip} of the piezoelectric metastructure. Block G represents the system plant, and variables d_i represent the disturbance vibrations acting within each unit cell i. The controller block has all non-diagonal terms equal to zero, as no coupling is present between the inputs and outputs of the different unit cells. This is also in line with the decentralised control architecture described.

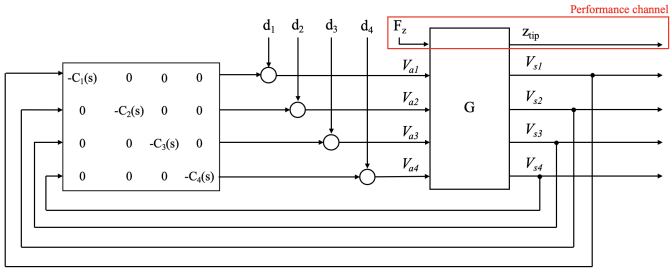

Fig. 2. Closed-loop block diagram of the decentralised control architecture used in active piezoelectric metamaterials.

Given such control architecture, the controllers $C_i(s)$ employed are pivotal in defining the unit cell dynamics and generating a bandgap. By looking at the transfer function between process disturbance d and system output y,

$$\frac{y}{d} = \frac{G}{1 + GC} \tag{3}$$

suitable controllers for bandgap generation can be selected. In particular, a controller with a resonance peak in its frequency response function is necessary such that, in closed-loop, this will result in an attenuation region. This is clear from Eq. (3), as a high gain in C at its tuned corner (resonant) frequency will result in a low magnitude in $\frac{y}{d}$, ultimately generating a vibration attenuation region.

In this paper, the bandgap generation performance of different controllers within metamaterial architectures is compared. The controllers chosen for evaluation are characterised by their simplicity and widespread use within the literature, as their tuning is not the primary focus of this study. Moreover, throughout this paper, the controllers that are deemed unfeasible for practical implementation within the presented metamaterial architecture will be systematically excluded. The first controller studied consists of a 2^{nd} order Low-Pass Filter (LPF) in which the sensed position signal is positively fed back into the system plant for control. Such a configuration is also known as Positive-Position-Feedback (PPF) control [13], and is commonly used in the literature for active damping applications in mechatronics [18] [19]. The second controller studied, instead, consists of a 2^{nd} order High-Pass Filter. This is often used in active damping applications for being the electrical realisation of a dynamic vibration absorber [20]. Its resonator-like characteristic makes it promising for bandgap generation in metamaterials. The last controller studied consists of a 2^{nd} order Band-Pass Filter (BPF), first used by Kim et al. [15] in narrowband position feedback for out-of-resonance vibration control. Indeed, based on the optimal results obtained on SDOF systems, its implementation within a metamaterial architecture is promising.

The transfer functions of the outlined controllers are,

$$LPF = -g \cdot \frac{\omega_c^2}{s^2 + 2\zeta\omega_c s + \omega_c^2} \tag{4}$$

$$HPF = k \cdot \frac{s^2}{s^2 + 2\zeta\omega_c s + \omega_c^2} \tag{5}$$

$$BPF = k \cdot \frac{2\zeta\omega_c s}{s^2 + 2\zeta\omega_c s + \omega_c^2} \tag{6}$$

where ω_c is the corner frequency of the filter (i.e., the frequency where the bandgap will be generated), ζ the damping ratio, g the gain of the LPF such that $0 < g < 1$, and k the gain of the HPF and BPF controllers such that $k > 0$. Note that, as previously mentioned, the LPF is implemented with positive feedback. Hence, for a negative feedback control loop such as that used in Fig. 2, the controller requires a negative sign to be used in positive feedback. With this in mind, it is clear that both HPF and BPF controllers are used in negative feedback.

C. Ideal implementation on simplified system model

As a preliminary analysis, the controllers without considering parasitic effects are tested using the simplified system introduced in Section II-A. Fig. 3 shows the resulting collocated transfer function obtained. Here, all controllers are tuned to generate a non-resonant bandgap at $\omega_c = 0.8$ rad/s, with the plant having a corner frequency of $\omega_n = 1$ rad/s, as mentioned previously. Here, it was observed that both the LPF and HPF controllers exhibit a resonance peak before the bandgap region. The reason for this is the steep slope of the second-order LP and HP filters at high and low frequencies, respectively. On the contrary, the 2^{nd} order BPF does not have such steep slopes, reason being it does not exhibit the resonance in the frequency response. In addition, the BPF is shown to be less effective in generating the desired bandgap due to a lower gain being used for closed-loop stability concerns.

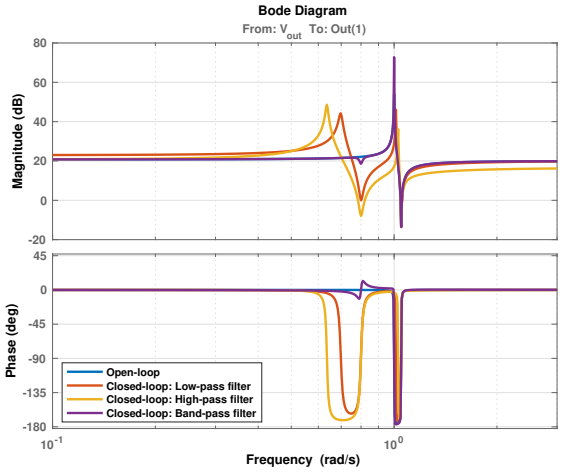

Fig. 3. Ideal bandgap generation of the different controllers on the simplified system. The collocated channel is shown.

Fig. 4 shows how a larger gain k for the BPF controller would lead to an unstable closed-loop response. Specifically, a higher controller

gain causes the resonance of the plant at 1 rad/s to be > 0 dB, thus causing the instability. These stability limitations are not ideal for practical implementation within active piezoelectric metamaterial architectures, as deep bandgaps are desired. Hence, the BPF controller will no longer be analysed in this paper. This stability concern does not arise when using the LPF and HPF controllers. The reason for this is that their loop transfer function is rotated by $\pm 90^{\circ}$ compared to that shown in Fig. 4, hence allowing for any gain to be used without causing stability issues in closed-loop. Further stability analyses and the parasitic dynamics that arise when dealing with piezoelectric transducers and experimental setups are studied in the next section.

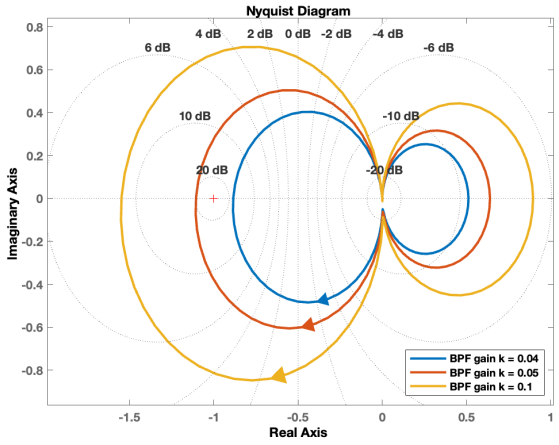

Fig. 4. Effect of a larger BPF gain k on the loop stability of the simplified system. The loop transfer function is stable when $k = 0.04$, and unstable when $k = 0.05$ and $k = 0.1$.

III. Parasitic Dynamics

When designing controllers and systems, the parasitic dynamics that might arise in an experimental setup and the effect these might have on the desired performance are often disregarded. Parasitic effects are present in all real-world systems and are troublesome to account for in the design phase. Within the precision industry, in particular, the effect of parasitic dynamics is further significant and cannot be neglected. In the case of this paper, the two most relevant parasitic effects when dealing with active piezoelectric metamaterials are 1. Time Delay, given the stability issues it can cause in the closed-loop of a system; and 2. the RC roll-off characteristic of piezoelectric transducers at low frequency. These are individually analysed in the following subsections.

A. Time Delay

Within an experimental setup, a computational delay is always present in the loop between sensor measurement, computer or data acquisition device, and controller output. A pure time delay T is characterised by a transfer function as,

$$D(s) = e^{-sT} \tag{7}$$

with constant magnitude and a phase lag $\phi = \omega T$ which increases linearly with frequency.

The effect of phase lag on the closed-loop performance of a system cannot be neglected, as it will inevitably decrease the phase margin, ultimately leading to instability. This is not a major concern for the LPF controller, as it exhibits a roll-off after its corner frequency ω_c. However, when considering the characteristics of a 2^{nd} order HPF controller with no roll-off after ω_c, the phase lag at higher frequencies can be detrimental. Specifically, the absence of roll-off causes the resonance of the plant ω_n to cross the 0 dB line in the loop transfer function, hence reducing its phase margin and suggesting instability in case of delay. This was modelled using the same simplified system introduced in Section II-A. Fig. 5 shows the effect of time delay on the loop stability when using a HPF controller. Here, it is observed how time delay (i.e., phase lag) causes a clockwise rotation of the loop transfer function in the Nyquist plot, ultimately causing it to encircle the (-1; 0) point and hence be unstable. Moreover, it is noted how the loop transfer function of a HPF controller with a phase lag of 90° is equivalent to that of a BPF controller (see Fig. 4). This further confirms the stability issues that can arise in case of delay on a closed-loop system with a HPF. Therefore, because Time Delay cannot be avoided in an experimental setup, but rather only compensated, the HPF controller is not feasible for practical implementation within active piezoelectric metamaterial architectures either, and thus no longer analysed in this paper. Note that compensating for this parasitic effect is challenging and would imply careful tuning of the controller; hence beyond the scope of this paper. Indeed, the PPF controller appears to be the most suitable out of the ones compared for practical implementation. This will be used for the remainder of the paper.

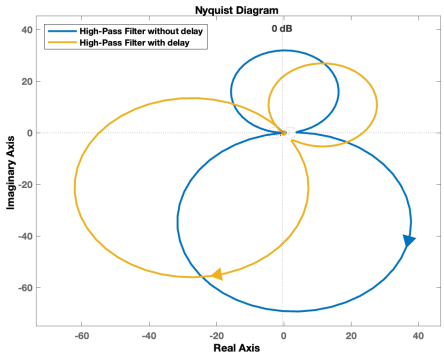

Fig. 5. Effect of Time Delay on the simplified system when using a HPF controller. The delayed system, in yellow, encircles the instability point. Without delay, in blue, this does not happen.

B. RC roll-off characteristics of piezoelectric sensors

Piezoelectric transducers are commonly used within the High-Tech industry for AVC applications. Their main advantages include [21]: high power density, fast response, large force, high sensitivity, small hysteresis, and stability. However, the inherent capacitance C of a piezoelectric material causes parasitic dynamics at low frequencies when combined with a resistive element R such as a data acquisition device or oscilloscope. Specifically, in sensing, the series connection of capacitance and resistance forms a potential divider which exhibits High-Pass (HP) characteristics with a corner frequency ω_{hp}. The magnitude of ω_{hp} can be easily calculated as

$$\omega_{hp} = \frac{1}{2\pi RC} \tag{8}$$

Typically, ω_{hp} has values in the low-frequency range. To study the effect of such HP behaviour on the bandgap-generation performance of active piezoelectric metamaterials, the simplified system introduced in Section II-A is used. Here, a HP filter with $\omega_{hp} = 0.1$ rad/s to mimic the effect of the parasitic dynamics is placed in series with the PPF controller (Eq. (4)). Fig. 6 shows the performance channel of the system when the controller with and without parasitic dynamics is implemented in the collocated transfer function from V_a to V_s. The controller's corner frequency was tuned for a non-resonant bandgap

at $\omega_c = 0.8$ rad/s. It is clearly observed how, despite $\omega_{hp} < \omega_c$, the HP behaviour of the piezoelectric sensor is not ideal, hence at ω_c the effects of the parasitic dynamics are still present and have an impact on the closed-loop response. In particular, a lower controller gain is required in order for the closed-loop response of the system to remain stable. Ultimately, this causes a reduction in the width and magnitude of the generated bandgap.

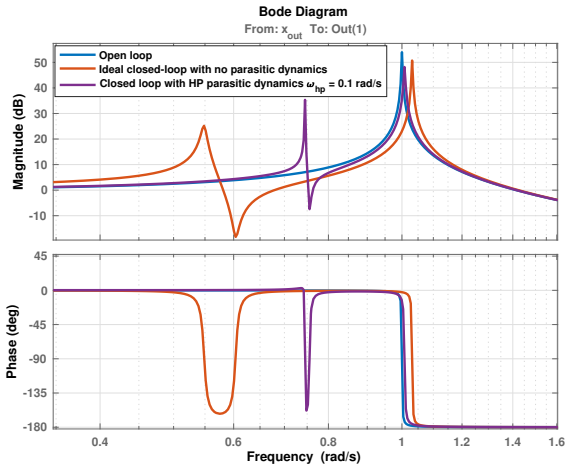

Fig. 6. Non-resonant bandgap: effect of parasitic dynamics comparison on a simplified system. The performance channel is shown.

To further study the impact of such parasitic behaviour, the influence of ω_{hp} on the closed-loop stability of the system for a non-resonant bandgap at $\omega_c = 0.8$ rad/s is assessed. Fig. 7 shows how the loop transfer function of the system changes for different values of ω_{hp} in the range $0.01 < \omega_{hp} < 0.2$ rad/s when the controller gain is unaltered and equal to $g = 0.2$. Here, it is observed how, as ω_{hp} increases closer to ω_c, the loop transfer function exhibits an increasing anti-clockwise rotation in the Nyquist plot, eventually leading to the encirclement of the (-1; 0) point and hence to instability. To compensate for this "rotation" towards instability, the easiest solution that does not involve complex tuning of the controller is to reduce its gain g.

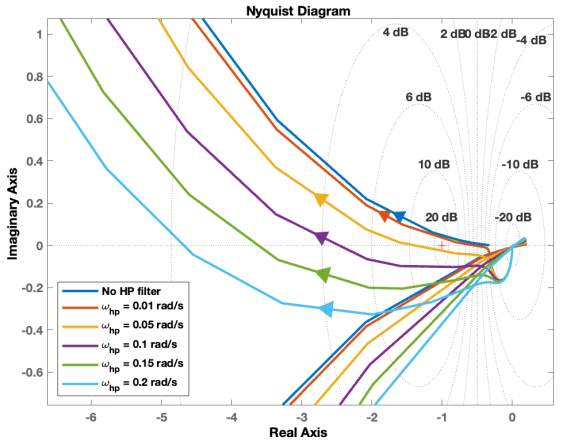

Fig. 7. Effect of ω_{hp} on the loop stability of the idealised system model. All loop transfer functions are unstable when $\omega_{hp} > 0.01$ rad/s.

However, as previously mentioned, reducing the controller's gain g causes a reduction of both the magnitude and the width of the generated bandgap. For the different values of ω_{hp} showed in Fig. 7, Fig. 8 shows the performance channel of the simplified system model after reducing the controller gains such that all closed-loops are stable. Indeed, it is observed how as ω_{hp} approaches ω_c, the controller gain needs to be gradually reduced and this causes the depth of the generated bandgap to progressively decrease. This also causes the progressive narrowing of the bandgap, as clearly observed in Fig. 8. The reason for this is that, at lower gains, a lower portion of the loop transfer function in the collocated channel crosses the 0 dB line at the target ω_c, hence reducing both the magnitude and width of the attenuation in the performance channel. However, a larger controller gain g also causes the bandgap to originate further away from the desired frequency $\omega_c = 0.8$ rad/s. The reason for this is that, with a larger g, the loop transfer function crosses the 0 dB line much before the targeted ω_c. For example, in Fig. 8, when $\omega_{hp} = 0.01$ rad/s, a gain $g = 0.5$ was used and the bandgap originated at around 0.55 rad/s. For $\omega_{hp} = 0.1$ rad/s, instead, a gain of 0.1 was used and the bandgap originated much closer to the target ω_c at around 0.75 rad/s.

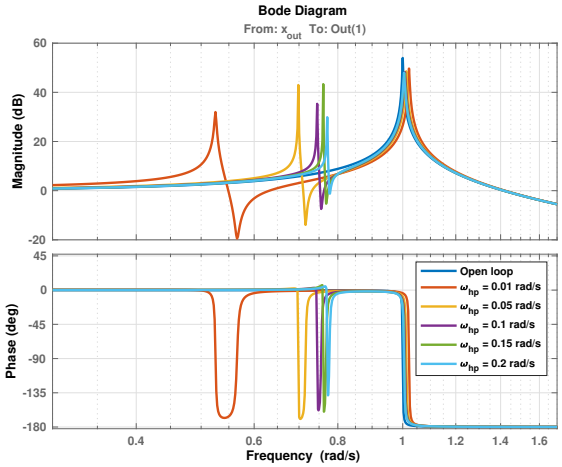

Fig. 8. Effect of ω_{hp} on generating a non-resonant bandgap at 0.8 rad/s. The performance channel is shown.

In the case of a resonant bandgap, instead, with parasitic dynamics $\omega_{hp} = 0.1$ rad/s and controller target corner frequency $\omega_c = \omega_n = 1$ rad/s, the effect of such parasitic characteristic is significantly different, as shown in Fig. 9. In fact, here, the exact same bandgap-generation capabilities are exhibited by the two systems with and without parasitic dynamics. The main reason for this is that the effect of the parasitic HP behaviour on the phase of the system is compensated by the increase in gain at the resonance. This was not the case for non-resonant bandgaps. An additional explanation is that at $\omega_c = 1$ rad/s, we are further away from the HP parasitic effect compared to the non-resonant bandgap case with $\omega_c = 0.8$ rad/s. Hence proving how if the controller is tuned to operate at a frequency $\omega_c >> \omega_{hp}$, then the parasitic effect becomes insignificant. However, in mechatronic precision systems, the low-frequency region is often of interest, reason being such a low-frequency parasitic effect is significant.

In general, the HP roll-off characteristic of piezoelectric transducers can have a significant impact on the bandgap-generation capabilities of active metamaterials, significantly limiting their performance especially if ω_{hp} is too close to ω_c. Therefore, the effect of such parasitic dynamics cannot be neglected and needs to be taken into consideration to accurately represent the dynamics of the experimental setup introduced in Section V. For this reason, the HP

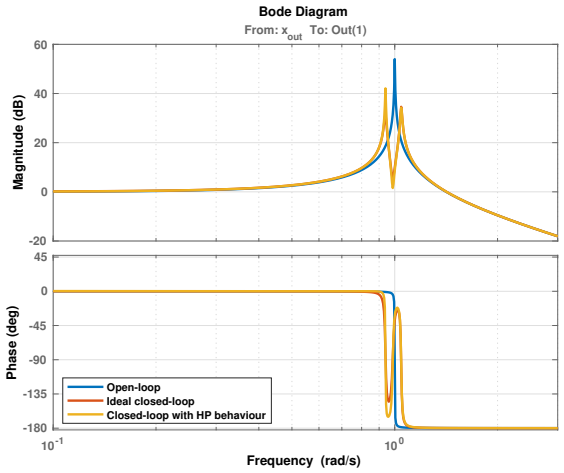

Fig. 9. Resonant bandgap: effect of parasitic dynamics comparison on a simplified system. The performance channel is shown.

parasitic effect will be modelled even in the more complex SPACAR system comprising multiple modes and unit cells, introduced in the following section.

IV. SPACAR Model Simulations

To accurately assess the bandgap-generation properties of active piezoelectric metamaterials, a more representative architecture of the experimental setup consisting of a 300 mm long, 35 mm wide, and 2 mm thick aluminium beam with 8 equally spaced unit cells is modelled in SPACAR. The collocated sensor-actuator piezoelectric transducers P-876.SP1 from PI are modelled in each unit cell, having a length of 16 mm, a width of 13 mm, and a height of 0.5 mm. Consecutive unit cells are 19.1 mm distant from one another. A position excitation is modelled at the base of the beam, and the resulting displacement at the tip is measured, constituting the performance channel $\frac{y}{d}$ of the modelled system. Moreover, a structural damping of 2.5% is assumed. The plane cantilever beam exhibits the first resonant mode at approximately 18 Hz, with the second one at 115 Hz. For the simulations presented in this section, non-resonant bandgaps are targeted at 60 Hz, whereas resonant bandgaps are tuned at the second mode of the system.

To accurately model the HP characteristic effect, the electrical capacitance of the piezoelectric transducers C is taken from their datasheet, equal to 8 nF [22]. Concerning the resistance R of the measuring device, instead, an effective value of 1 MΩ is assumed. This is often the case when using oscilloscopes or data acquisition devices [23]. Hence, using Eq. (8), ω_{hp} is estimated to be around 20 Hz. This value will therefore be used to model the parasitic dynamics in this section. Specifically, the HP behaviour is added to the collocated channels of the system, where piezoelectric sensor measurements are made.

Fig. 10 shows the performance channel of the full SPACAR model for a target non-resonant bandgap at 60 Hz. Here, it is observed that the system with parasitic effects only shows a small dip at 60 Hz, and does not generate the desired bandgap. The reason for this is in accordance with the findings of Section III; as the HP behaviour requires a reduction in the controller gain in order for the stability of the closed-loop to be maintained. Ultimately, this gain is too small for an observable bandgap to be generated in the performance channel. On the contrary, the 'ideal' system with no parasitic effects shows the desired non-resonant bandgap with a 10 dB attenuation. As previously explained, the large controller gain causes the bandgap to generate at a frequency of approximately 48 Hz, slightly lower than the targeted 60 Hz. Moreover, it is observed how the shape of the non-resonant bandgap for the full SPACAR model is different compared to that in Fig. 6 for the simplified system. Specifically, the SPACAR model exhibits an additional resonance peak after the bandgap, and not only before it, as was the case in Fig. 6. This is caused by the larger number of modes and couplings present in the SPACAR model, which affect the closed-loop dynamics and lead to the resonances both before and after the generated bandgap.

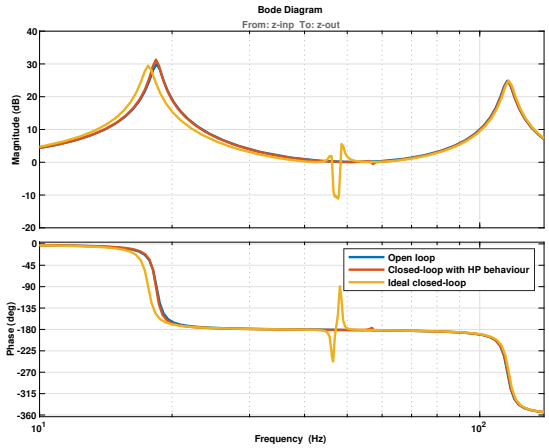

Fig. 10. Non-resonant bandgap: effect of parasitic dynamics comparison on a full SPACAR model. The performance channel is shown.

In the case of a resonant bandgap at 115 Hz, instead, Fig. 11 shows the obtained performance transfer function for systems with and without parasitic effects. Indeed, in accordance with the results from Section III, both the ideal and parasitic systems exhibit the same closed-loop response and generate the desired bandgap. The comparable response of the two systems on the full SPACAR model with multiple modes and coupling is very promising for the resonant bandgaps that can be attained using the experimental setup. These results are presented and discussed in the following section.

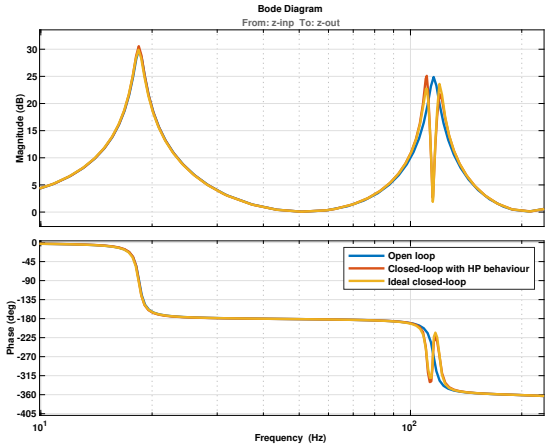

Fig. 11. Resonant bandgap: effect of parasitic dynamics comparison on a full SPACAR model. The performance channel is shown.

V. Experimental Results

The complete SPACAR system model outlined in Section IV is converted into an experimental setup as shown in Fig. 12. Here, the aluminium beam-like structure is fixed at the base through a clamping mechanism. To do so, the total length of the beam is required to be > 300 mm, such that the additional segment can be clamped through a set of machine screws. To provide the external force disturbance F_z at the base of the beam, the P-887.31 stack actuator from PI is used. This is pre-loaded using a machine screw on the opposite side of the structure for proper functioning, and an amplified operating voltage of $0 - 50$ V is tuned. At the top end of the beam, instead, the tip displacement z_{tip} is measured using the Micro-Epsilon optoNCDT 1900 position sensor. The high linearity and resolution (0.1μm) of the sensor allows for accurate displacement measurements to be made. Therefore, the beam's length of 300 mm is taken from the tip of the beam to the position of the stack actuator. As previously outlined, the transfer function from z_{tip} to F_z defines the performance channel of the system where the bandgaps ought to be observed. The 8 unit cells of the metastructure, equally distributed along the beam's length, are also observed in Fig. 12. The control signals for the actuators V_{ai} are generated by digital controllers and BD 300 voltage amplifiers, tuned for an output voltage of ± 50 V. Enamelled copper wire with a diameter of 0.32 mm are soldered to the piezoelectric patches, with Thorlabs supports used for accurate management and guiding of these wires. LabView software and a CompactRIO NIc-RIO 9039 chassis are used to log sensor data at 10 kHz and compute output control signals for the collocated actuators in the unit cells. Likewise, the same CompactRIO computes the chirp disturbance signal sent to the stack actuator at the base.

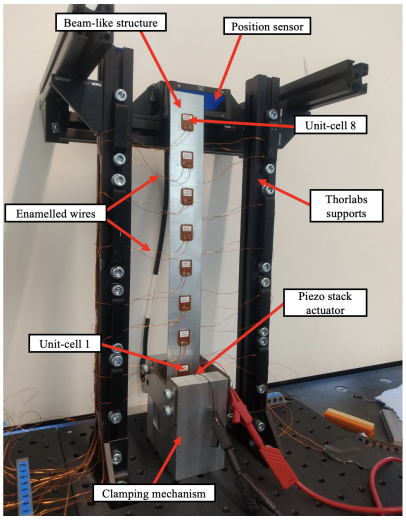

Fig. 12. Experimental setup used.

For the piezoelectric sensors, a 16-bit NI 9215 Analogue Input module is used, with a resistor of $R = 1$ MΩ between each differential analogue input. Considering the electrical capacitance of the piezoelectric sensors used (8 nF), this confirms the assumptions made in Section IV, with an expected High-Pass parasitic effect of corner frequency $\omega_{hp} = 20$ Hz. Moreover, the experimental setup is identified in the frequency region of interest with a chirp signal from 10 Hz to 200 Hz, such as to reduce computational efforts. The identified experimental plant exhibits its first mode at 18 Hz, and the second resonant frequency at 110 Hz. These frequencies closely match those of the SPACAR model outlined in Section IV, with no discrepancy on the first resonant frequency and only a 5 Hz discrepancy on the second one. The reason for the discrepancy could be different material properties of the beam or a different structural damping. Nonetheless, the experimental results further validate the accuracy of the designed SPACAR system model.

For a targeted non-resonant bandgap at 60 Hz, Fig. 13 shows the obtained results using the experimental setup of Fig. 12. Indeed, as expected from the non-resonant bandgap using the full SPACAR model in Fig. 10, the HP parasitic effect of the piezoelectric sensors does not allow for a bandgap to generate in the performance channel of the experimental setup. The reason for this is consistent with that previously explained throughout the paper so far, as a lower gain g is required for the controller, at which no observable bandgap can generate. Moreover, in Fig. 13, a slope of -2 is observed. The reason for this is that a position sensor is used for tip displacement rather than an accelerometer, as is a common convention within the literature [24]. Force input and acceleration output are commonly used given their direct relation resulting in a slope of zero in the transfer function. However, for a position output, a double integration (from acceleration) is required, which in turn causes the -2 slope. In the SPACAR model, for instance, the transfer function in Fig. 10 has no slope as it is from position input at the base to position output at the tip.

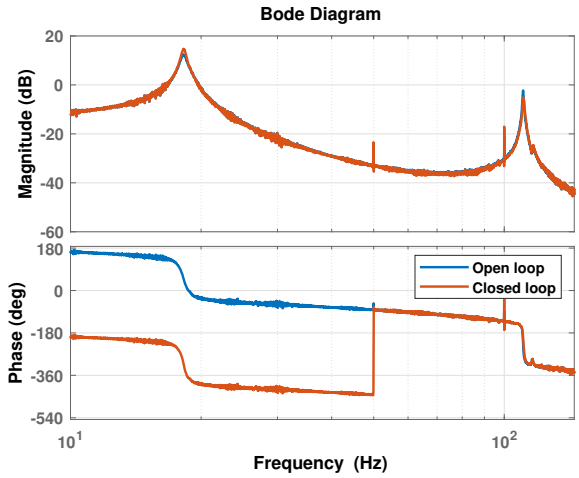

Fig. 13. Non-resonant bandgap at 60 Hz on the experimental setup. The performance channel is shown.

In the case of a resonant bandgap at 110 Hz, Fig. 14 shows the obtained experimental results. Here, the desired bandgap generated at the second resonant frequency of the experimental system is successfully obtained. Moreover, the obtained bandgap is analogous to that attained on the full SPACAR model shown in Fig. 11. Indeed, this further validates the previously presented analyses regarding the effect of parasitic dynamics on the resonant bandgap generation capabilities of the system. Most importantly, this proves the effectiveness of the designed system in generating bandgaps. In fact, by appropriately countering the HP parasitic dynamics, it is expected for the same bandgap generation capabilities to be attained at lower frequencies, closer to ω_{hp}.

To this aim, an 'intermediate' bandgap was tested using the experimental setup. Specifically, the controller was tuned for the lowest value of ω_c in the range $60 < \omega_c < 110$ Hz such that a bandgap was observed within the performance channel of the system. Fig. 15 shows the obtained performance channel for an intermediate bandgap at 90 Hz. As expected, the attenuation provided by the bandgap is limited, given the small gain g used. Nonetheless, the bandgap is made observable in the performance channel. This is promising as it confirms the hypothesis that by compensating for the parasitic HP behaviour of the piezoelectric sensors, bandgaps can be generated even at lower (non-resonant) frequencies near ω_{hp}.

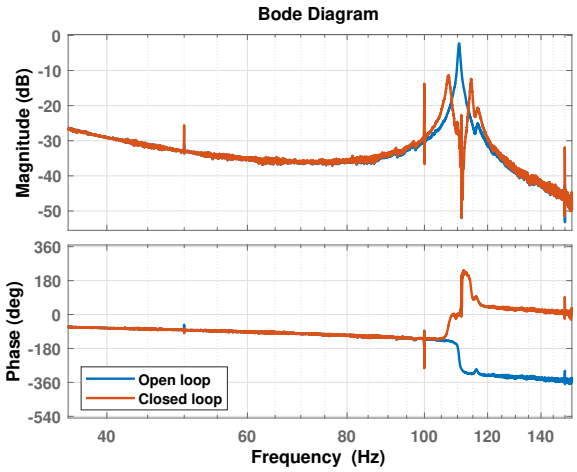

Fig. 14. Resonant bandgap at 110 Hz on the experimental setup. The performance channel is shown.

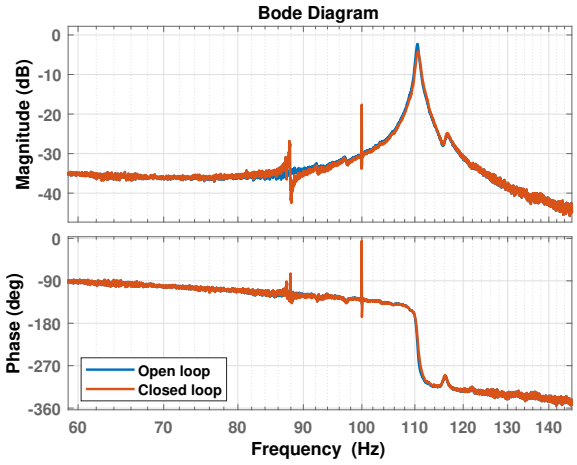

Fig. 15. Intermediate bandgap at 90 Hz on the experimental setup. The performance channel is shown.

Indeed, the results from Fig. 15 and Section IV suggest that non-resonant bandgaps can be attained using metamaterial architectures by compensating the HP parasitic dynamics caused by the piezoelectric transducers. Different methods are possible to compensate for such parasitic effects, with the most common being the implementation of charge amplifiers. Charge amplifiers' main function is to produce a suitable voltage output proportional to the charge of the sensor by integrating the generated current. This ultimately allows for an improvement of the measurements in the low-frequency range, which is where the parasitic effect ω_{hp} typically is. Alternatively, different methods such as sensor fusion to improve the quality of the low-frequency measurements can be adopted. Regardless of the method chosen, compensation for such a parasitic effect is necessary if a non-resonant, low-frequency bandgap is desired using active piezoelectric metamaterials.

VI. Conclusion

This paper investigates the practical issues involved in the implementation of active piezoelectric metamaterials for the generation of resonant and non-resonant bandgaps in beam-like structures. Three different controllers were analysed. Band-Pass Filter controllers were found to be sub-optimal given stability limitations when using large gains. Similarly, High-Pass Filter controllers were not suitable given their instability in case of parasitic dynamics such as time delay. Overall, Positive Position Feedback controllers were found to be the most effective out of the ones compared in generating bandgaps. Additional parasitic effects such as the RC roll-off of piezoelectric sensors were also studied. This was found to be significant in limiting the bandgap generation capabilities of the system in the non-resonant regions. In fact, non-resonant bandgaps were not attained in the implemented metamaterial architecture. The reason for this was the added phase caused by the HP behaviour, which required a reduction in controller gain for stability and ultimately reduced the bandgap performance. This was not the case for resonant bandgaps, as the parasitic phase lead was compensated by the increase in gain at the resonance, ultimately allowing for optimal resonant bandgaps to be generated. The experimental setup was first modelled in SPACAR and subsequently built to confirm such results. An 'intermediate' bandgap was also observed suggesting how by compensating the studied parasitic dynamics a non-resonant bandgap can be generated as well. Lastly, methods for compensating for such parasitic dynamics were briefly proposed.

Future work for this research is clear and consists in implementing one of the proposed methods to compensate for the limitations imposed by the RC roll-off of piezoelectric transducers.

References

[1] M. B. S.M. Kim, S.J. Elliott, "Decentralised control for multichannel active vibration isolation," *Control Systems Technology*, vol. 9, pp. 93–100, 2001.

[2] G. H. C.-T. S. R. Zhu, X. Liu and G. Huang, "Negative refraction of elastic waves at the deep-subwavelength scale in a single-phase metamaterial," *Nature Communications*, vol. 5, p. 5510, 2014.

[3] J. X. M. A. W. S. C. S. N. Fang, D. Xi and X. Zhang, "Ultra-sonic metamaterials with negative modulus," *Nature Materials*, vol. 5, no. 6, p. 452, 2006.

[4] C. Sugino, S. Leadenham, M. Ruzzene, and A. Erturk, "On the mechanism of bandgap formation in locally resonant finite elastic metamaterials," *Journal of Applied Physics*, vol. 120, no. 13, p. 134501, 10 2016.

[5] Y. M. Y. Y. Z. Z. Y. C. T. C. Z. Liu, X. Zhang and P. Sheng, "Locally resonant sonic materials," *Science*, vol. 289, pp. 1734–1736, 2000.

[6] F. L. C. Z. Shuaimin Haoa, Zhijing Wua, "Enhancement of the band-gap characteristics in disordered elastic metamaterial multi-span beams: Theory and experiment," *Mechanics Research Communications*, vol. 113, 2021.

[7] C. Sugino and Y. Wang, "Dynamics of mechanical and electromechanical locally resonant metastructures," *Georgia Institute of Technology*, 2019.

[8] U. Aridogan and I. Basdogan, "A review of active vibration and noise suppression of plate-like structures with piezoelectric transducers," *Journal of Intelligent Material Systems and Structures*, pp. 1455–1476, 2015.

[9] S. C. Gang Wang, "Large low-frequency vibration attenuation induced by arrays of piezoelectric patches shunted with amplifier-resonator feedback circuits," *Smart Material Structures*, vol. 25, pp. 15–30, 2016.

[10] A. M. Baz, "An active acoustic metamaterial with tunable effective density," *ASME. J. Vib. Acoust.*, vol. 4, p. 132, 2010.

[11] X.-N. Zhao, X.-D. Yang, W. Zhang, and H. Pu, "Active tuning of elastic wave propagation in a piezoelectric metamaterial beam," *AIP Advances*, vol. 11, no. 6, p. 065009, 06 2021.

[12] L. Ning, Y.-Z. Wang, and Y.-S. Wang, "Active control cloak of the elastic wave metamaterial," *International Journal of Solids and Structures*, vol. 202, pp. 126–135, 2020.

[13] J. L. Fanson and T. K. Caughey, "Positive position feedback control for large space structures," *AIAA Journal*, vol. 28, no. 4, pp. 717–724, 1990.

[14] B. M. Kim S., Wang S., "Comparison of negative and positive position feedback control of a flexible structure," *Smart Material Structures*, vol. 20, pp. 96–103, 2011.

[15] M. J. B. S. M. Kim and G. L. Abreu, "Narrowband feedback for narrowband control of resonant and non-resonant vibration," *Mechanical Systems and Signal Processing*, vol. 76 - 77, pp. 47 – 57, 2016.
[16] A. Preumont, *Vibration Control of Active Structures: An introduction*. Springer International Publishing, 2018.
[17] J. Lunze, "Feedback control of large scale systems," *Prentice Hall PTR*, 1992.
[18] J. F. A. Baz, S. Poh, "Independent modal space control with positive position feedback," *Journal of Dynamic Systems, Measurement, and Control*, vol. 114, pp. 96–103, 1992.
[19] F. J. E. M. Anderson EH, Moore DM, "Development of an active member using piezoelectric and electrostrictive actuation for control of precision structures," *AIAA Journal*, 1990.
[20] D. H. J. P, *Mechanical Vibration*. New York: McGraw-Hill, 1947.
[21] G. Barac, "Multimode damping with activated metamaterials," 2020.
[22] PI, "Dura act patch transducer," www.physikinstrumente.com/datasheets/P-876-Datasheet.pdf, 2023.
[23] S. F. M. Specialities, "Piezo film sensors technical manual," https://www.sparkfun.com/datasheets/Sensors/Flex/MSI-techman.pdf, 1999.
[24] O. J. Kim S, "A modal filter approach to non-collocated vibration control of structures," *Journal of Sound and Vibration*, vol. 332, pp. 2207 – 2221, 2013.

Chapter 4

Compensating Parasitic Dynamics

As studied in the previous chapter, the parasitic effects encountered in the practical implementation of active piezoelectric metastructures can significantly limit their bandgap generation performance. For this reason, adequate solutions are required. Regarding the influence of time delay, this is less significant on the system performance given the effect is particularly strong at higher frequencies, whereas the controllers target lower frequency regions. Moreover, the effect of delay on PPF controllers was observed to be minimal. Hence, this parasitic effect is not discussed in this chapter.

On the contrary, the impact of the RC roll-off characteristic of piezoelectric transducers is much more significant. How this works is that the inherent capacitance C of a piezoelectric material causes parasitic dynamics at low frequencies when combined with a resistive element R such as a data acquisition device or oscilloscope. In sensing, the series connection of capacitance and resistance forms a potential divider which exhibits High-Pass (HP) characteristics with a corner frequency ω_{hp}. The magnitude of ω_{hp} can be easily calculated as

$$\omega_{hp} = \frac{1}{2\pi RC} \tag{4.1}$$

Here, the phase lead caused by the HP behaviour requires a reduction in controller gain in order for the stability of the closed loop to be maintained, ultimately reducing the performance of the generated bandgap. In the remainder of this chapter, possible ways to avoid and compensate for such parasitic effect are discussed.

4.1 Experimental setup

One solution to avoid such parasitic effect, without compensating for it, would be to push ω_{hp} to lower values. This way, the influence of such parasitic dynamics on the controller bandwidth region would be reduced. To achieve this, the inherent capacitance C of the transducers can be increased. It is known that the capacitance of an element increases when the plate area increases [47], hence using larger piezoelectric transducers offers a viable solution. For instance, P-876.A11

transducers from PI have a much larger piezoelectric area, with a length of 61 mm, and a width of 35 mm. This allows for them to have an inherent capacitance of $C = 150$ nF [48], which is much larger compared to the 8 nF of the currently used P-876.SP1 transducers. Ultimately, by using Eq. (4.1), the newly introduced piezoelectric patches would have a value of ω_{hp} approximately equal to 1 Hz. This constitutes a massive improvement when compared to the value of 20 Hz attained by using the current transducers.

However, such a solution is not feasible for the present study. The main reason for this is that substituting the current piezoelectric patches with higher capacitance ones would imply building a completely new setup from scratch. This is obviously not convenient, especially when considering time and costs. Moreover, simulations using the current 300 mm long, 35 mm wide beam-like structure are not feasible with the higher capacitance transducers in a 7-unit cell configuration, as they will not fit in terms of length. Therefore, either a different-sized beam structure or a lower number of unit cells would be required, which would make the comparison with the current setup unfair. Hence, such a comparison is not conducted. Nonetheless, based on the theory of capacitance and piezoelectric transducers, it is indeed expected for the newly suggested patches to reduce the RC roll-off parasitic dynamics.

4.2 Charge Amplifiers

Alternatively, as discussed in Chapter 3, another viable solution to compensate for such parasitic behaviour consists of the implementation of charge amplifiers. The main function of a charge amplifier is to produce a voltage output proportional to the charge of the piezoelectric sensor by integrating the generated current. Most importantly, this allows for quasi-static measurements and generally improves the low-frequency data acquisition of the sensor, which is where the parasitic effects of the transducers are observed, hence presenting charge amplifiers as a promising solution for this problem. Additional advantages come from the implementation of charge amplifiers but are not mentioned here for the sake of brevity.

Figure 4.1 illustrates the circuit diagram schematic for a charge amplifier. Here, V_{cc} is the voltage supplied to the op-amp, V_o is the amplifier's output voltage, C_f is the feedback capacitor used for integration, and R_i is the input resistor to avoid electrostatic discharge. Lastly, R_f is the feedback resistor in parallel with C_f, providing the discharge path to prevent saturation.

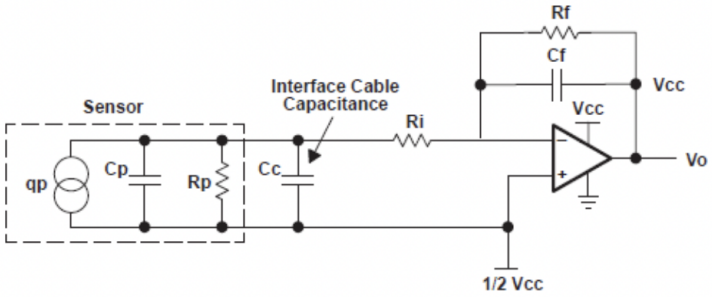

Figure 4.1: Charge amplifier circuit diagram [49].

In tuning such a charge amplifier configuration, its bandwidth is important. This defines the region of influence of the amplifier. Specifically, the charge amplifier will act from a frequency

(in Hz) of $\omega_1 = 1/(2\pi R_f C_f)$ to $\omega_2 = 1/(2\pi R_i (C_p + C_c))$, with a gain equal to $1/C_f$ in the bandpass region in-between. Hence, given that the HP parasitic behaviour of the piezoelectric transducers occurs at low frequencies, ω_1 is the most important parameter. In particular, it is required for $\omega_1 << \omega_{hp}$, such that the amplifier operates in the same frequency range as the parasitic dynamics and compensates for them.

In the following subsection, the preliminary results obtained when the outlined charge amplifier circuit is implemented are shown. Being preliminary results, the charge amplifier circuit is implemented only for the first unit cell of the experimental setup.

4.2.1 Initial Testing

For practical implementation in the experimental setup, the TL072CP operational amplifier from TI was used, with a voltage supply V_{cc} of ± 10 V. It is known that $\omega_{hp} = 20$ Hz, as mentioned in Section 4.1. Therefore, to ensure the proper functioning of the charge amplifier circuit and attain $\omega_1 << \omega_{hp}$, a corner frequency of 1 Hz was targeted for ω_1. To achieve this, adequate values of R_f and C_f were selected based on the availability of components within the mechatronics lab. Specifically, three resistors were connected in series such that the total $R_f = 2$ MΩ, and two capacitors were connected in parallel such that the sum $C_f = 82$ nF. Using these parameters, the desired value of $\omega_1 = 0.97$ Hz ≈ 1 Hz was achieved. It is important to note that such analysis is part of the initial tests made to improve the built setup in the lab. Therefore, the implementation and tuning are not perfect or professional but the setup is fully functioning.

Fig. 4.2 shows the breadboard implementation of the charge amplifier circuit (in Fig. 4.1) using the components outlined above. Labels are added for clarity. For initial testing and analyses, the charge amplifier is implemented only for the first unit cell of the metamaterial architecture. Hence, for a full system implementation, a circuit like that in Fig. 4.2 is required for each of the 7 piezoelectric sensors in the metastructure. Within the experimental setup, the charge amplifier circuit is placed between the sensor and the data acquisition device. Fig. 4.3 shows a schematic of this for better understanding purposes. Here, the voltage generated by the piezoelectric sensor V_{s1} is fed to the charge amplifier, which in turn conditions the measurement signal and feeds a voltage V_o to the data acquisition module.

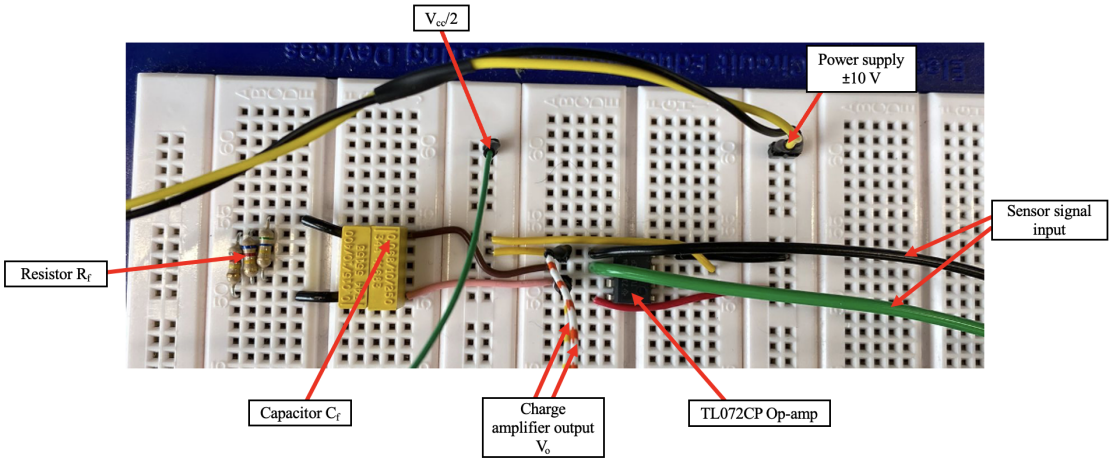

Figure 4.2: Charge amplifier circuit on a breadboard in the lab.

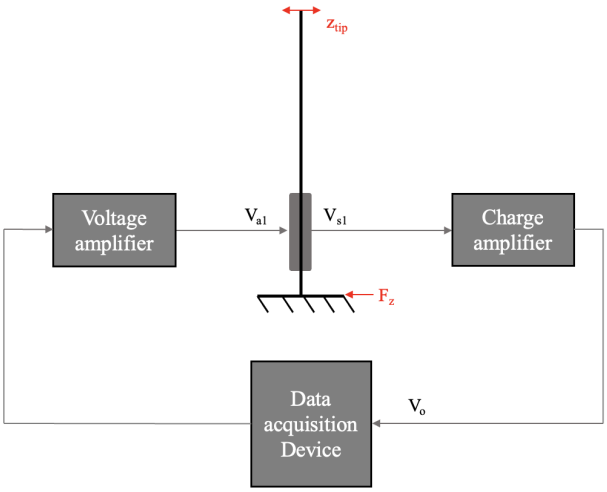

Figure 4.3: Schematic showing the location of the charge amplifier circuit within an arbitrary metamaterial configuration.

To test the performance of the implemented charge amplifier in suppressing the HP parasitic behaviour of the piezoelectric sensors, the collocated transfer function from actuator 1 (V_{a1}) to sensor 1 (V_{s1}) was identified again. Fig. 4.4 shows the obtained result in comparison with the old transfer function without the charge amplifier. The same sampling time and chirp signal increase rate were used to allow for a more fair comparison. Indeed, the performance improvement is noticeable; as the RC roll-off of the piezoelectric transducers is completely compensated by the charge amplifier. Specifically, in the non-resonant bandgap target frequency of 60 Hz, no phase lead is observed, thus suggesting a greater stability margin when the controller is implemented.

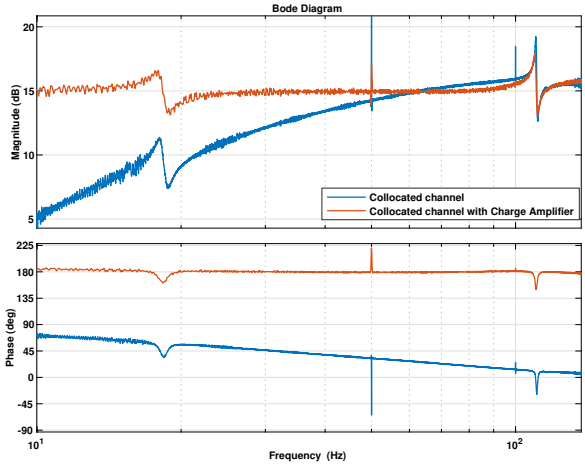

Figure 4.4: Collocated transfer function of unit-cell 1 in the metastructure with and without charge amplifier circuit.

The result is extremely promising as the HP behaviour is compensated both in terms of gain and phase in the identified Bode plot. Consequently, by equipping each unit cell of the metastructure with a suitable charge amplifier circuit, it is expected for the parasitic dynamics to be completely eliminated from the system. As a result, a high gain can be employed by the controllers to generate non-resonant bandgaps in the performance channel without concerns regarding loop stability. The potential full implementation of such charge amplifier circuits are discussed in greater detail in Section 5.2.

Chapter 5

Conclusions and Recommendations

5.1 Conclusions

In this thesis, the objective of investigating the practical issues involved in the experimental implementation of active piezoelectric metamaterials for both resonant and non-resonant vibration suppression is fulfilled.

To do so, the effectiveness of three different controllers in generating bandgaps was analysed, and the influence of parasitic dynamics on their performance was studied. Band-Pass Filter controllers were found to be generally sub-optimal given the stability issues encountered when using large controller gains. Similarly, Negative Position Feedback controllers were not suitable given their instability in the case of parasitic dynamics such as time delay, which cannot be avoided in an experimental setup and are difficult to compensate for. Overall, Positive Position Feedback controllers were found to be the most effective out of the ones compared in generating bandgaps. Additional parasitic effects such as the RC roll-off of piezoelectric sensors was also studied. This was found to be significant in affecting the non-resonant bandgap generation capabilities of the system. In fact, non-resonant bandgaps were not attained in the studied metamaterial architecture. The reason for this was the added phase caused by the HP parasitic behaviour, which required a reduction in controller gain for stability and ultimately reduced the bandgap performance. Such behaviour was not observed in the case of resonant bandgaps, as the phase lead was compensated by the increase in gain at the resonance. This allowed for optimal resonant bandgaps to be generated in the setup.

Additional analyses were made to suggest how, by compensating the parasitic effects of the piezoelectric transducers, effective non-resonant bandgaps can also be attained in the metamaterial architecture. In this respect, the initial tuning and implementation of charge amplifier circuits are described. The clear improvements following their implementation in the experimental setup are also shown, further suggesting the outlined hypothesis.

To achieve the described results and conclusions, a simplified metamaterial model consisting of a single mode and unit cell was initially used. Subsequently, a full experimental architecture was modelled in SPACAR, and the effect of parasitic dynamics was simulated for accurate prediction

of experimental results. The modelled experimental architecture was consequently built and utilised in the mechatronics lab for active bandgap implementation. Indeed, when parasitic effects were modelled, the system in SPACAR was found to closely represent the experimental setup built, both in terms of closed- and open-loop results.

To further validate the conclusions and attain non-resonant bandgaps by using the experimental setup, additional research and work is required. This is extensively outlined in the following section.

5.2 Recommendations and Future steps

No research can ever be considered complete or perfect. Hence, recommendations for improvement and future steps are always possible. In this section, these are thoroughly discussed for the conducted study.

5.2.1 Improvements of Experimental Setup

In this subsection, recommendations related to the possible improvements that can be made in the existing experimental setup to improve the quality of the attained results are discussed. In general, these do not require major changes or extensions to the already existing setup.

The first suggested improvement relates to the data acquisition process, which can be improved at the cost of larger computational efforts. Note that the suggested improvements in this paragraph are trivial for mechatronic engineers, but nonetheless are mentioned as they are currently not tuned for maximum performance given the limited computational effort and time available throughout the conducted thesis. The process pursued to acquire data from the experimental setup is thoroughly explained in Appendix C. In this respect, the acquisition of data can be made more accurate in a number of ways. For instance, setting a smaller sampling time such as 10 ms (instead of 100 ms) would allow for a sampling rate of 100 kHz, 10 times larger than the currently used 10 kHz. Ultimately, this would imply a large number of samples acquired per second and a better representation of the system's response. However, this would also logically be more expensive in terms of data storage and handling. Another example would be setting a lower increase rate for the chirp signal used in the identification process. Currently, the frequency is swept at an increase rate of 1%; further reducing this would allow for more accurate identification at each frequency, with lower background noise. Indeed, this would also significantly increases the identification time, reason being an increase rate of 1% was found to be a good compromise for the conducted study.

Another useful improvement to the experimental setup concerns the voltage amplifiers used for the actuators. Currently, PiezoDrive BD 300 voltage amplifiers are used. Despite being efficient in that they take up a significantly small amount of space in the lab setup (see Appendix A), these are not the most suitable in terms of output noise. In fact, these have an accuracy of 1% over a full output range of ± 300 V [50]. Numerous voltage amplifiers are present on the market with significantly higher accuracy. For instance, Piezoelectric Smart Materials' High Voltage Amplifiers (HVA) EEL 1500-1 are a viable improvement. Specifically, these have an accuracy of 0.1% over a full output range of ± 1000 V [51]. Indeed, the improvement would be significant and would allow for a reduction in the noise being transmitted to and measured by the piezoelectric sensors when the actuators are excited. The main reason why the PiezoDrive BD300 amplifiers were used in the setup was, other than their compact size, their high availability in the mechatronics lab.

Additionally, regarding the amplifier used for the piezoelectric stack in the setup, PiezoMechanik's LE 150/200 HVA would be more suitable compared to the BD 300. This is because, although the voltage signal for the stack actuator was accurately tuned such as to be within the targeted operating range of $0 - 50$ V, the suggested amplifier allows for greater robustness in this respect by having a unidirectional output voltage range of -10 V to $+500$ V. This is because the voltage amplifier proposed is specifically targeted for use with piezoelectric stacks. In the case of this study, such an amplifier was not used to be consistent with the rest of the experimental setup.

5.2.2 Extensions of Experimental Setup

In this subsection, the extensions that can be added to the experimental setup such as to achieve proper non-resonant bandgaps are discussed. The term 'extensions' refers to additional components or circuits that can be added to the setup.

The first extension proposed is a natural follow-up of the conducted research, and consists in implementing the charge amplifiers presented in Chapter 4 for all the unit cells of the metastructure. In this respect, initial tuning, testing, and results have already been presented for one unit cell. The suggested way of doing this in the case of multiple unit cells would be that of designing a Printed Circuit Board (PCB) with interchangeable capacitors and resistors such as to allow for the corner frequency ω_1 of the charge amplifier to be adjusted. This way, the PCB would be extremely versatile and could be used for multiple applications and different setups. Indeed, specific tuning for the individual collocated transfer functions of the metastructure would also be possible, thus further improving the quality of the obtained results. Furthermore, as outlined in Chapter 4, such an implementation is promising regarding the potential non-resonant bandgaps that can be attained in the metamaterial structure.

It is possible for the expected performance of the charge amplifiers to not always be as perfect or ideal as that presented in Chapter 4. Reasons for this might be the ageing of circuit components, interference, or other parasitic effects that might arise during practical implementation for all unit cells. To account for this, an additional extension is proposed consisting of a compensator to combine in series with the controller. This would have a transfer function of $\frac{s+\omega a}{s+\omega/a}$. At high frequencies, the compensator has a gain of 1, such that its impact on the closed-loop performance is negligible. At lower frequencies, a gain of a^2 is observed instead. At the compensator's corner frequency ω, a phase lag is added with both width and depth proportional to a. This added phase lag would be useful in case the charge amplifier does not fully compensate for the parasitic phase lead caused by the piezoelectric transducers. The flexibility of the compensator through the tuning of the parameters a and ω makes this optimal for practical implementation in the system. For instance, with a value of $a = 1.1$, a maximum phase lag of 5° is observed at ω, which would be enough to allow for the stability of the closed-loop at a certain controller gain g.

An additional, more time-consuming extension consists in using sensor-fusion strategies to improve the quality of the measured signals. As studied, it is clear by now that the quality of the low-frequency measurements made by the piezoelectric transducers can be improved. Hence, a solution would be using a different sensor which is specialised in lower-frequency measurements, and fusing the information obtained with that from the piezoelectric sensor. This way, the information from the additional sensor is used in the low-frequency range, whereas that of the current piezoelectric sensor is used for higher frequencies. For this purpose, strain cells can be a viable option, given their typical low corner frequency. In this case, the implementation would require the sensor to be positioned close to the piezoelectric transducer, one for each unit cell, such that the observability of the sensors is the same. Indeed, this is the most difficult extension proposed in this subsection, but nonetheless a viable option for extending the current setup and allowing

for non-resonant bandgaps to be attained. Moreover, adequate tuning for the proper fusion of the sensor information is required.

5.2.3 Future Steps

In this subsection, the future steps that can be followed regarding the research conducted are discussed. Overall, these are suggested only after the previously outlined improvements and extensions are made. In particular, note that the future steps proposed still revolve around the built setup, as a significant amount of work and research can still be performed by using it.

Assuming the successful implementation of the improvements and extensions proposed in the previous subsections, one possible direction for the conducted research can be that of focusing more on the controllers implemented within the unit cells. Within this research, as clearly outlined in Chapter 3, simple and widely used controllers were purposely employed, as their tuning was not the main focus of the study. Hence, future work can certainly be made in finding the "optimal" controller for implementation within these active piezoelectric metastructures. In this respect, performance metrics can be set such as to evaluate performance based on the depth of the bandgap, its width, and the spillover effects caused. Dynamic Error Budgeting can also be used to more accurately assess the performance of the controllers in reducing the transmission of vibrations.

Moreover, using the built metamaterial architecture, methods to make the generated bandgaps wider can also be studied in the future. Within the literature, the field of graded and rainbow metamaterials is extensively studied [52] [53] [54] [55] [56], and results seem promising in this area for generating wide vibration attenuation regions using metamaterial architectures. In graded metamaterials, a constant (linear) frequency spacing, δ, between the natural frequencies of neighbouring local resonators is introduced, such as to enlarge the generated bandgaps or potentially generate multiple ones. Indeed, given the flexibility of such active metamaterial architecture, changes in the corner frequencies of the controllers in the unit cells can be easily made to attain the desired graded metastructures.

Lastly, future work can be done using the metamaterial architecture by implementing modal filters. Here, these can be designed such that each unit cell of the metamaterial sees only one mode, and subsequently controls it. This way, by implementing active damping controllers, the modes of the system can be individually targeted and damped. The fact that 7 unit cells are available in the current setup allows for a significant number of modes to be targeted simultaneously.

Bibliography

[1] A. Preumont, *Vibration Control of Active Structures: An introduction.* Springer International Publishing, 2018.

[2] M. B. S.M. Kim, S.J. Elliott, "Decentralised control for multichannel active vibration isolation," *Control Systems Technology*, vol. 9, pp. 93–100, 2001.

[3] S. M. Kim, S. Pietrzko, and M. J. Brennan, "Active vibration isolation using an electrical damper or an electrical dynamic absorber," *IEEE Trans. Control Syst.Technol*, vol. 16, pp. 245–254, 2008.

[4] G. H. C.-T. S. R. Zhu, X. Liu and G. Huang, "Negative refraction of elastic waves at the deep-subwavelength scale in a single-phase metamaterial," *Nature Communications*, vol. 5, p. 5510, 2014.

[5] J. X. M. A. W. S. C. S. N. Fang, D. Xi and X. Zhang, "Ultra-sonic metamaterials with negative modulus," *Nature Materials*, vol. 5, no. 6, p. 452, 2006.

[6] C. Sugino, S. Leadenham, M. Ruzzene, and A. Erturk, "On the mechanism of bandgap formation in locally resonant finite elastic metamaterials," *Journal of Applied Physics*, vol. 120, no. 13, p. 134501, 10 2016.

[7] F. L. C. Z. Shuaimin Haoa, Zhijing Wua, "Enhancement of the band-gap characteristics in disordered elastic metamaterial multi-span beams: Theory and experiment," *Mechanics Research Communications*, vol. 113, 2021.

[8] C. Sugino and Y. Wang, "Dynamics of mechanical and electromechanical locally resonant metastructures," *Georgia Institute of Technology*, 2019.

[9] S. C. Gang Wang, "Large low-frequency vibration attenuation induced by arrays of piezoelectric patches shunted with amplifier-resonator feedback circuits," *Smart Material Structures*, vol. 25, pp. 15–30, 2016.

[10] A. M. Baz, "An active acoustic metamaterial with tunable effective density," *ASME. J. Vib. Acoust.*, vol. 4, p. 132, 2010.

[11] X.-N. Zhao, X.-D. Yang, W. Zhang, and H. Pu, "Active tuning of elastic wave propagation in a piezoelectric metamaterial beam," *AIP Advances*, vol. 11, no. 6, p. 065009, 06 2021.

[12] "Active control cloak of the elastic wave metamaterial," *International Journal of Solids and Structures*, vol. 202, pp. 126–135, 2020.

[13] J. L. Fanson and T. K. Caughey, "Positive position feedback control for large space structures," *AIAA Journal*, vol. 28, no. 4, pp. 717–724, 1990.

[14] J. F. A. Baz, S. Poh, "Independent modal space control with positive position feedback," *Journal of Dynamic Systems, Measurement, and Control*, vol. 114, pp. 96–103, 1992.

[15] B. M. Kim S., Wang S., "Comparison of negative and positive position feedback control of a flexible structure," *Smart Material Structures*, vol. 20, pp. 96–103, 2011.

[16] M. J. B. S. M. Kim and G. L. Abreu, "Narrowband feedback for narrowband control of resonant and non-resonant vibration," *Mechanical Systems and Signal Processing*, vol. 76 - 77, pp. 47 – 57, 2016.

[17] J. D. Joannopoulos, S. G. Johnson, J. N. Winn, and R. D. Meade, *Photonic Crystals*. Princeton Univ. Press, 2007.

[18] M. S. Kushwaha, P. Halevi, L. Dobrzynski, and B. Djafari-Rouhani, "Acoustic bandstructure of periodic elastic composites," *Physical Review Letters*, vol. 71, no. 13, p. 2022, 1993.

[19] R. A. Shelby, D. R. Smith, and S. Schultz, "Experimental verification of a negative index of refraction," *Science*, vol. 292, no. 5514, pp. 77–79, 2001.

[20] J. Li and C. T. Chan, "Double-negative acoustic metamaterial," *Physical Review E*, vol. 70, no. 5, pp. 505–602, 2004.

[21] X. Liu, T. Tyler, T. Starr, A. F. Starr, N. M. Jokerst, and W. J. Padilla, "Taming the blackbody with infrared metamaterials as selective thermal emitters," *Physical Review Letters*, vol. 107, no. 4, p. 045 901, 2011.

[22] Z. Liu, X. Zhang, Y. Mao, Y. Y. Zhu, Z. Yang, C. T. Chan, and P. Sheng, "Locally resonant sonic materials," *Science*, vol. 289, pp. 1734–1736, 2000.

[23] S. Huber, "Mechanical metamaterials," *ETH Zurich*, vol. 10, 2018.

[24] [Online]. Available: https://theconstructor.org/structural-engg/tuned-mass-damper/1198/

[25] C. Sugino and Y. Wang, "Dynamics of mechanical and electromechanical locally resonant metastructures," *Georgia Institute of Technology*, vol. 9, 2019.

[26] K. j. C. J. Yu, C. Nerse and S. Wang, "A framework of flexible locally resonant metamaterials for attachment to curved structures," *International Journal of Mechanical Sciences*, vol. 204, no. 8, 2021.

[27] U. Aridogan and I. Basdogan, "A review of active vibration and noise suppression of plate-like structures with piezoelectric transducers," *Journal of Intelligent Material Systems and Structures*, pp. 1455–1476, 2015.

[28] G. Barac, "Multimode damping with activated metamaterials," Master's thesis, *TU Delft*, 2020.

[29] M. G. Soto and H. Adeli, "Multi-agent replicator controller for sustainable vibration control of smart structures," *Journal of Vibroengineering*, pp. 4300–4322, 2017.

[30] S. O. R. Moheimani and A. J. Fleming, *Piezoelectric transducers for vibration control and damping*. Springer, 2006.

[31] R. M. Schmidt, G. Schitter, A. Rankers, and J. van Eijk, "The design of high performance mechatronics," *Delft University Press*, vol. 3, p. 437, 2018.

[32] C. Sugino and Y. Wang, "Dynamics of mechanical and electromechanical locally resonant metastructures," *Georgia Institute of Technology*, vol. 41, 2019.

[33] C. Vasques and J. D. Rodrigues, "Vibration and structural acoustics analysis," 2011.

[34] R. Grip, *Vibration and noise control using shunted piezoelectric transducers: A review.* Mechanical Systems and Signal Processing, 2018.

[35] J. Lunze, *Feedback control of large scale systems.* PTR: Prentice Hall, 1992.

[36] C. Sugino and Y. Wang, "Dynamics of mechanical and electromechanical locally resonant metastructures," *Georgia Institute of Technology*, pp. 23–29, 2019.

[37] D. L. Platus, "Negative-stiffness-mechanism vibration isolation systems," *SPIE—Vibration Control in Microelectronics, Optics and Metrology*, vol. 1619, pp. 44–54, 1991.

[38] J. Zhang, D. Li, and S. Dong, "An ultra-low frequency parallel connection nonlinear isolator for precision instruments," *Key Engineering Materials*, vol. 257, pp. 231–236, 2004.

[39] M. A. Beijen, M. F. Heertjes, H. Butler, and M. Steinbuch, "Disturbance feedforward control for active vibration isolation systems with internal isolator dynamics," *Journal of Sound and Vibration*, vol. 436, pp. 220–235, 2018.

[40] M. A. Beijen, J. V. Dijk, W. B. J. Hakvoort, and M. F. Heertjes, *Self-tuning Feedforward Control for Active Vibration Isolation of Precision Machines.* IFAC, 2014.

[41] M. A. Beijen, M. F. Heertjes, J. V. Dij, and W. B. J. Hakvoort, "Self-tuning mimo disturbance feedforward control for active hard-mounted vibration isolators," *Control Engineering Practice*, vol. 72, pp. 90–103, 2018.

[42] S. M. Kim, S. Wang, and M. J. Brennan, "Dynamic analysis and optimal design of a passive and an active piezo-electrical dynamic vibration absorber," *J. SoundVib*, vol. 330, pp. 603–614, 2011.

[43] F. J. L and C. T. K, "Positive position feedbackcontrol for large space structures," *AIAA*, vol. 28, pp. 717–724, 1990.

[44] P. S. Kim S M and B. M. J, "Active vibration isolation using an electrical damper or an electrical dynamic absorber," *IEEE Trans. Control Syst. Technol.*, vol. 16, pp. 245–254, 2008.

[45] V. B. J. G. Moheimani S O R and B. B, "Experimental implementation of extended multivariable ppf control on an active structure," *IEEE Trans. Control Syst.Technol.*, vol. 14, pp. 443–455, 2006.

[46] D. H. J. P, *Mechanical Vibration.* New York: McGraw-Hill, 1947.

[47] S. Tutorials, "Capacitors," [Online] Available: https://learn.sparkfun.com/tutorials/capacitors/all#:~:text=The%20capacitance%20of%20a%20capacitor,1mF)%20is%20a%20big%20capacitor.

[48] PI, "Dura act patch transducer," 2023, [Online] Available: https://www.physikinstrumente.com/fileadmin/user_upload/physik_instrumente/files/datasheets/P-876-Datasheet.pdf.

[49] J. Karki, "Signal conditioning piezoelectric sensors," tech. rep., 2000," [Online]. Available: https://www.ti.com/lit/an/sloa033a/sloa033a.pdf.

[50] P. Drive, "Bd300, bd250, bd200, bd150: Dual channel drivers for piezo bender actuators," [Online] Available: https://www.piezodrive.com/wp-content/uploads/2021/01/BD300-V5-Datasheet-R6.pdf.

[51] E. E. L. S. Material, "Eel1500-1 user manual," [Online] Available: https://www.smart-material.com/media/Manuals/EEL1500-1-V1-WEB2021.pdf.

[52] G. Hu, A. C. M. Austin, V. Sorokin, and L. Tang, "Metamaterial beam with graded local resonators for broadband vibration suppression," *Mechanical Systems and Signal Processing*, vol. 146, 2021.

[53] M. B. Assouar, J. H. Sun, F. S. Lin, and J. C. Hsu, "Hybrid phononic crystal plates for lowering and widening acoustic band gaps," *Ultrasonics*, vol. 54, no. 8, pp. 2159–2164, 2014.

[54] R. Khajehtourian and M. Hussein, "Nonlinear locally resonant metamaterials: Modeling and dispersion characteristics," *Proceedings of Phononics*, pp. 180–181, 2013.

[55] M. Brennan, "Characteristics of a wideband vibration neutralizer," *Noise Control Engineering Journal*, vol. 45, no. 5, pp. 201–207, 1997.

[56] H. Meng, D. Chronopoulos, A. T. Fabro, W. Elmadih, and I. Maskery, "Rainbow metamaterials for broadband multi-frequency vibration attenuation: Numerical analysis and experimental validation," *Journal of Sound and Vibration*, vol. 465, 2020.

Appendix A

Experimental Setup

In this appendix chapter, the experimental setup used is thoroughly explained and shown. The components are accurately described and the arrangement of the setup within the Mechatronics Lab is outlined.

A list of all the necessary components to replicate the experiments conducted is outlined in Tbl. A.1. In Fig. A.1, a picture of the whole working setup in the Mechatronics Lab is shown. Labels are added to illustrate the way the components were positioned. Fig. A.2, instead, shows a close-up picture of the metamaterial architecture used and the respective components.

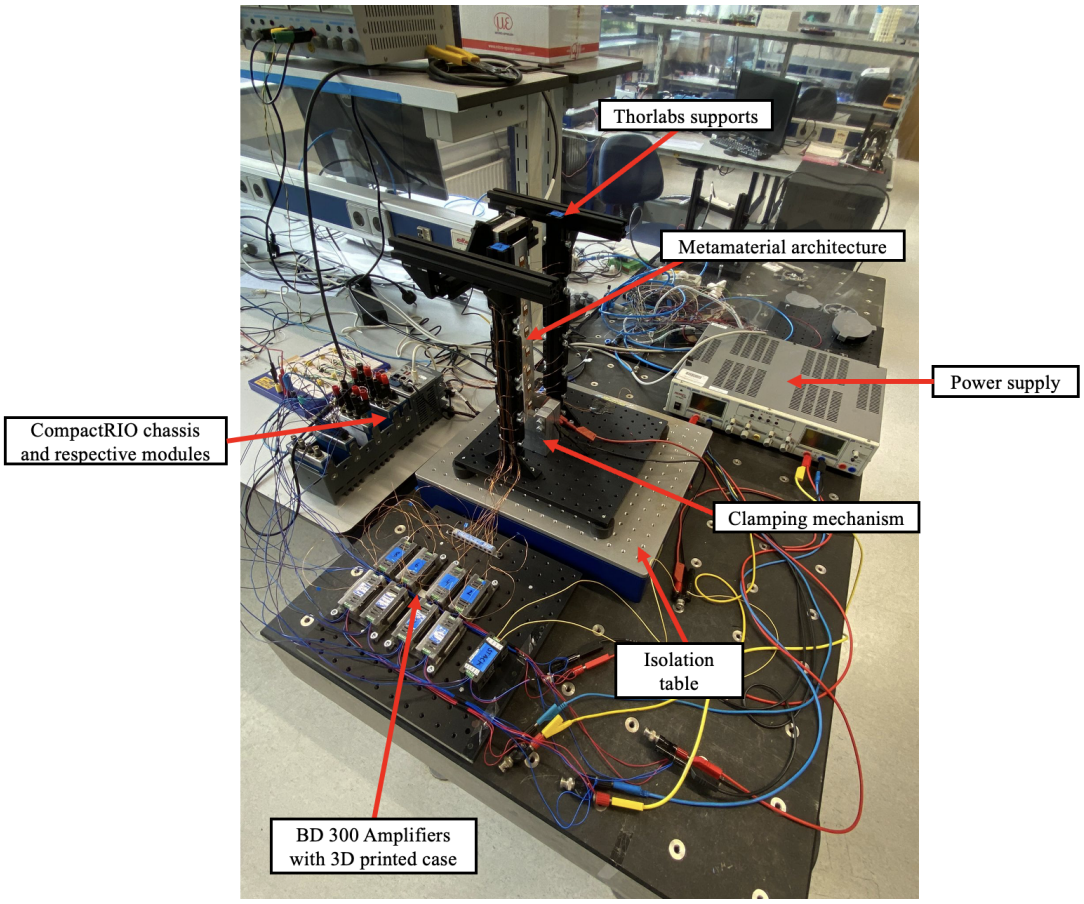

Figure A.1: Overview illustration of the experimental setup used.

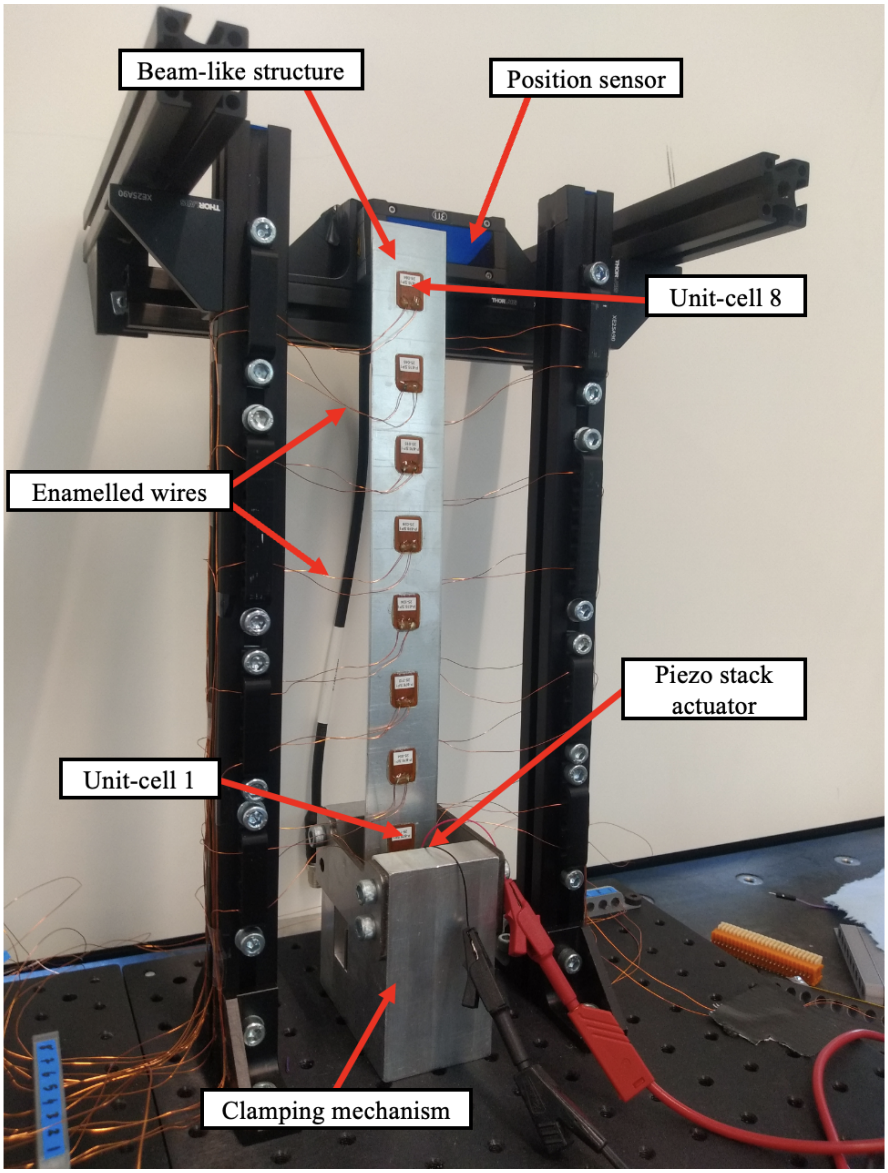

Figure A.2: Close-up of the experimental metamaterial architecture used.

Table A.1

Component	**Details**	**Function**
Beam structure	Aluminium, 300x35x2 mm	Structure used in the experiments to represent beam-like systems. Quantity: 1.
Clamping mechanism	Aluminium, machine screws and bolts	Firmly fix the beam at the base to create a cantilever. Also includes a machine screw to pretension the stack actuator. Quantity: 1.
Position sensor	Micro-Epsilon optoNCDT 1900	Optical sensor used to measure the displacement in the transverse direction at the tip of the beam - performance channel output. Quantity: 1.
Piezoelectric stack actuator	PI P-887.31 (3x3x13.5 mm)	Externally excite the base of the cantilever beam in the transverse direction - performance channel input. Quantity: 1.
Piezoelectric benders	PI P-876.SP1 (13x16x0.5 mm)	Piezoelectric transducers used as sensors (8) and actuators (8) for active vibration control of the beam. A sensor-actuator pair forms a unit cell. Eight unit cells in total were used. Quantity: 16.
Voltage Amplifier	PiezoDrive BD300	Amplify the voltage signal sent to the piezoelectric stack (1) and the piezoelectric transducers in actuation mode (8). Quantity: 9.
Controller	NI CompactRIO (cRIO-9047)	Obtain sensor measurement data, compute control voltage (action) based on the control algorithms implemented, log and store data. Quantity: 1.
Analogue Input Module	NI 9215 (16-bits, 4-Channel C Series Voltage Input Module)	Obtain sensor measurement data. Wires are connected from the sensor to the module, which is in turn placed within the cRIO chassis. Quantity: 2.
Analogue Output Module	NI 9264 (16-bits, 16-Channel C Series Voltage Output Module)	Apply disturbance and control voltage to the piezoelectric stack and transducers. Wires are connected from the module to the respective voltage amplifiers for the actuators. The module itself is also placed within the cRIO chassis. Quantity: 1.
Wires	Enamelled copper wires (Diameter = 0.32 mm)	Connect the system. Used because of their light weight and hence minimal impact on the system. Furthermore, easy to solder on the small piezoelectric transducers. Average length of each wire: 120 cm.
Power Supply	24 V - max 5 A	Power the voltage amplifiers and opto-position sensor (24 V). Quantity: 1.
Support structure	Thorlabs	Used for accurate management and guiding of the wires, and for supporting the optical position sensor at the tip of the structure.
Vibration isolation table	Table-Stable TS-150	Isolate external vibrations for repeatable measurements and lowering external noise.

Appendix B

Practical Work

In this appendix chapter, the practical work involved in the building of the experimental setup is outlined. This serves as a guide should an individual want to recreate the setup, and includes general useful advice when dealing with piezoelectric transducers (both in gluing and soldering them).

B.1 Gluing piezoelectric transducers

To build the 8-unit-cell metamaterial architecture used in the experiments, the piezoelectric transducers needed to be glued precisely on the 300x35x2 mm aluminium beam structure such as to have collocated actuator-sensor pairs. To achieve this, a mask was designed for the beam on an arbitrary CAD software. In this case, for simplicity and time constraints, the mask was printed in 2D on paper. If desired, the same process can also be done using a 3D printer and PLA material. Once the paper mask was printed and cut out, this was precisely attached onto the aluminium beam using tape. Fig. B.1 shows the printed paper mask attached to the beam structure, where the holes represent where the piezoelectric benders should be glued on the beam. Logically, these were made 0.1 mm larger than the actual dimension of the transducers, to allow for some tolerance in gluing.

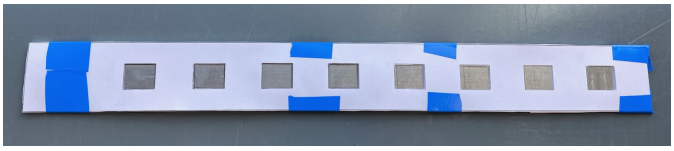

Figure B.1: Paper mask taped (in blue) to the aluminium beam structure for precise gluing of the piezoelectric benders.

Because paper is not ideal when dealing with epoxy glue, the paper mask was used to make pencil markings onto the structure to indicate where the piezoelectric transducers should be glued, and then removed when the actual gluing process took place. Hence, once all 8 positions were marked on one side of the beam using the printed paper mask, the gluing process began. For this, epoxy glue was used. In particular, *Double Bubble Loctite* epoxy glue (see Fig. B.2), as it was found to be the most suitable for this application. The two components of the epoxy glue (Part A and Part B) were mixed in a 1:1 ratio, and could be processed for approximately 3-5 minutes before hardening. In this time frame, for a meticulous job to be done, it is suggested to glue no more than 2 piezoelectric patches at a time. Hence, multiple batches of epoxy glue need to be mixed.

Figure B.2: Epoxy used to glue the piezoelectric benders onto the aluminium beam host structure.

Specifically, for every piezoelectric bender on the beam, once its position was determined using the paper mask designed, the following gluing procedure was used.

1. Clean both the surface of the beam and that of the piezoelectric bender using ethanol to remove any dirt.

2. Mix the two components of the epoxy glue (Part A and Part B) in a 1:1 ratio on a mixing palette.

3. Apply a thin layer of glue on the piezoelectric bender and evenly distribute it across the entirety of its gluing surface area.

4. Apply another thin layer of glue on the aluminium beam in the designated position where the piezoelectric patch is desired to be glued.

5. Position the patch in the desired location on the beam and gently press on top of it to make any excess glue come out from underneath it.

6. Wet a clean paper towel with ethanol and remove the excess glue from the four edges of the piezoelectric patch. Be aware that the patch will move during this process, but this is fine as long as you re-position it correctly.

7. Fix the piezoelectric patch in position using removable tape.

8. If necessary, remove once again any excess epoxy using a paper towel and ethanol.

9. Place a few pieces of paper on top of the glued area and position a heavy flat object on top of it (e.g., a few large textbooks, or a metal block) to ensure the patch is uniformly glued to the beam.

10. Ensure the weights are on top of the patch for at least 15 minutes.

11. After 15 minutes, the weights can be removed together with the pieces of paper and the removable tape.

12. Inspect the glued piezoelectric bender. As a rule of thumb, if a small layer of epoxy glue is observed on each side of the transducer, the latter can be assumed to be glued correctly and uniformly.

13. Repeat steps 1 - 12 for every piezoelectric patch you wish to glue on the structure. Remember to do a maximum of 2 patches at a time given the time constraints imposed by the epoxy glue used.

Fig. B.3 shows the desired end-product after the gluing process outlined in this subsection. Once one side of the aluminium beam was done (i.e., all piezo-benders were glued onto it), the process outlined in this sub-section was repeated in exactly the same manner for the other side of the beam. This also meant that the same paper mask was used for this purpose. This way, a metamaterial with 8 exactly collocated unit cells was made.

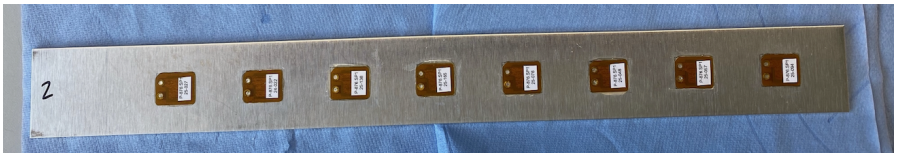

Figure B.3: End-product of the piezoelectric patches glued onto the aluminium beam host structure.

B.2 Soldering wires to piezoelectric transducers

In order to connect the piezoelectric transducers to the system, electrical wires are required. For this purpose, enamelled copper wires were used. The main advantage of this type of wire is its lightweight, hence allowing it to have minimal impact on the system. Moreover, as relatively small transducers were used (16x13x0.5 mm), this type of wire was more suitable and easy to solder. However, it is important to mention that such wire is available in only one colour, hence making it difficult for one to distinguish which wire goes to which sensor/actuator. A colour-coding system can be useful for this purpose. In the case of the experimental setup used in this report, a colour code was not necessary as significant care was taken with regard to wire management, to ensure wires could clearly be distinguished and identified. The specific enamelled copper wire used in this case had a diameter of 0.32 mm. Fig. B.4 shows the spool of enamelled wire used in the experimental setup.

Figure B.4: Spool of enamelled copper wire with diameter equal to 0.32 mm used to connect the piezoelectric transducers in the experimental setup.

For every piezoelectric bender on the beam, the following procedure was used to solder the enamelled copper wires. Note how each patch had a positive and negative connection.

1. Cut the enamelled copper wire of the desired length (approximately 120 cm is an adequate wire length for the experimental setup used).
2. Remove the coating from the wire using fine sandpaper. Do this only at the ends of the wire for logical safety reasons.
3. Clean the soldering points on the piezoelectric patches using a cotton swab (or any similar alternative) and acetone. This will remove any excess epoxy that might have deposited on them during the gluing process, and hence avoid burning it and ruining the soldering surface. This step is extremely important!
4. With both ends of the wire prepared, and the soldering surface free of any remaining epoxy glue, heat the soldering iron at approximately 300°C.
5. Add tin to the soldering iron and deposit this on the connection pad of the piezoelectric patch together with the enamelled wire. Do not leave the soldering iron on the piezoelectric patch for too long - 1 second should be more than enough.
6. The wire should now be nicely connected to the piezoelectric transducer. Ensure the connection is solid and the soldering is finished.
7. Repeat steps 1-6 for all the wires that need to be connected to the piezoelectric transducers in the experimental setup.

If the steps are followed accurately, Fig. B.5 shows the desired end-product.

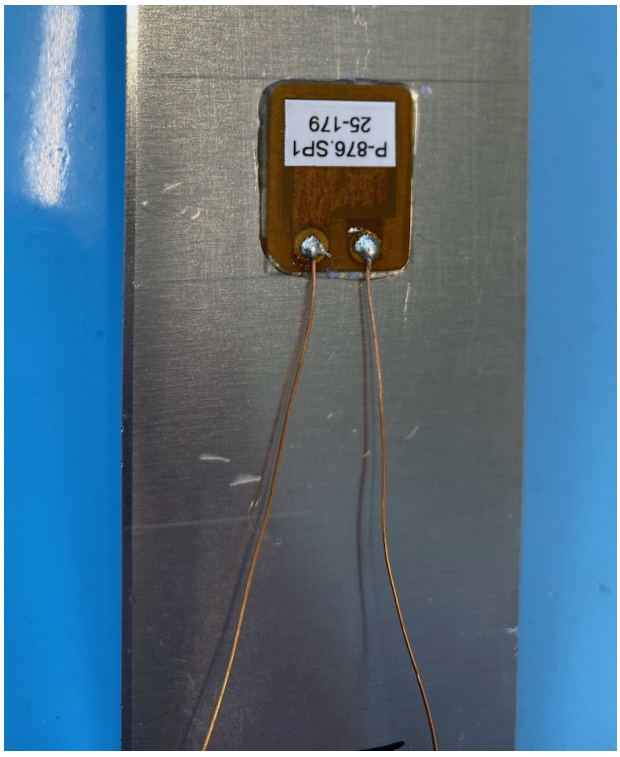

Figure B.5: End-product of the soldered enamelled copper wires on the piezoelectric transducer.

The system is now ready to be used, but for an optimal functioning setup one last step is necessary. This involves covering the soldered connection points of the piezoelectric transducers with a thin layer of epoxy glue. The reasons for doing this are two:

- **Safety:** the layer of epoxy will completely isolate the soldered connection points and hence avoid the risk of being electrocuted;

- **System robustness:** the layer of epoxy will avoid any risk of the soldered connection points jumping off the structure in case of abrupt movement or wire stretch.

The process is straightforward if the detailed guidelines on how to handle Epoxy glue found in Appendix B.1 are followed. An important remark for this task is to ensure that the glue does not cover the active piezo-ceramic area of the transducer. This is because an uneven distribution of epoxy glue on the transducer might cause some issues with its proper functioning and performance. An ideal result is displayed in Fig. B.6

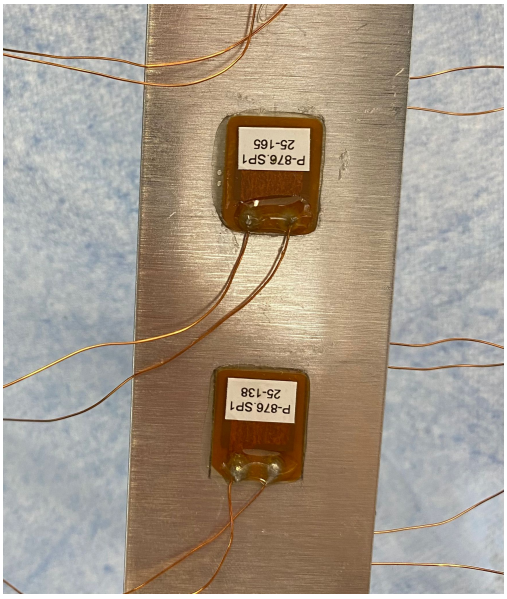

Figure B.6: Ideal end result of epoxy glue applied on the soldered connection points of piezoelectric transducers.

Appendix C

Software

In this appendix chapter, a guideline and overview of the software used in combination with the experimental setup is provided. First, the LabView files and code used for the identification and implementation of control algorithms are outlined. Secondly, the code and method used to post-process the data from the experimental setup in Matlab is explained.

C.1 LabView project

Within the LabVIEW project used for this thesis, there are three important files, namely FPGA.vi, RTMain.vi, and Host.vi. The FPGA file includes the control algorithm that is running on the compactRIO chassis. If one wishes to change the control algorithm or the FPGA.vi file in general, a compilation will be necessary. This usually takes about 30 minutes. Hence, changes to this file need to be made strategically. The RTMain.vi file acts as an interface between the computer and the compactRIO chassis. Here, variables from the FPGA.vi can be changed, and these changes do not require compilation, but rather take a few seconds. Therefore, it is ideal for commonly-changed variables to be placed within this file. The Host.vi file, instead, runs entirely on the computer. The main function of such file is that of collecting and saving data on the hard disk of the laptop. The data can then later be used for post-processing. Fig. C.1 shows a schematic representation of these three main files.

Figure C.1: Schematic showing the interface between FPGA, RTMain, and Host VIs in LabVIEW.

To run the LabVIEW project, the files should be run in the following order: FPGA.vi, RTMain.vi, and lastly Host.vi. To stop running the project, instead, the STOP button should be used for the RTMain.vi and Host.vi, in any order, and lastly the FPGA.vi should be stopped by using the "Abort Execution" button. In the following sub-sections, the contents of each of the presented files used for this thesis project are explained.

C.1.1 FPGA VI

In the FPGA.vi, for identification purposes, it is necessary for a chirp signal (sinusoid disturbance) to be generated and sent to either the stack at the base or the actuators in the collocated unit cells of the metastructure. For this purpose, the code in Fig. C.2 is used. Depending on whether the chirp is sent to a collocated actuator or the stack, different variables are used. The "*Offset*" parameter determines the offset of the generated chirp signal. This is set in bits, hence if an offset of 1.5 V is desired, the corresponding value in bits needs to be inputted. The relation between the bits and the output voltage can be easily determined knowing that the output module has 16-bits and an analogue output of ± 10 V. The bi-directional output voltage means there are $2^{15} = 32768$ bits in each direction (both positive and negative). To account for an unsigned bit (i.e., 0 V), we need to subtract one and this yields 32767 bits to represent voltages in the range 0-10 V. Hence, if a desired voltage offset of 1.5 V is desired, for instance, the corresponding bit value will be $\frac{32767*1.5}{10} = 4915$ bits. The "*Amplitude Factor*" parameter, instead, scales the amplitude of the generated sinusoidal signal. If, as a simple example, a sinusoidal amplitude of 1.5 V is desired, then an amplitude factor of $\frac{32767}{4915} = 35.8 \approx 36$ is required, where we know 4915 bits correspond to 1.5 V and 32767 bits correspond to 10 V. The upper and lower limits of the sinusoid are also set in bits, and are there to avoid damaging components in case something goes wrong. The frequency of the chirp signal is in fixed point value, hence if a signal of 10 Hz is desired, a value of 10 needs to be input. When the Boolean "*Stack on*" is true, the tuned chirp signal is sent to the piezoelectric stack actuator.

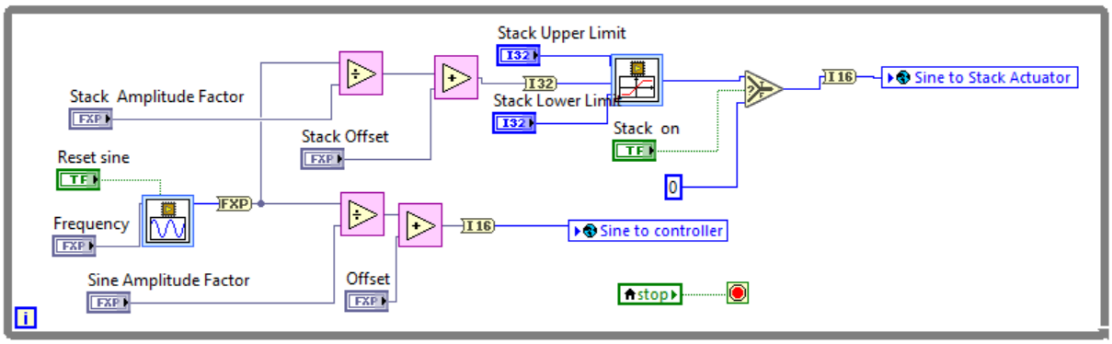

Figure C.2: How the chirp signal is generated in the FPGA.vi file in LabVIEW.

The sensor data for the computation of the control algorithm is collected by the NI 9215 modules, as previously outlined in Appendix A. To acquire the data from the sensor in the FPGA.vi, the LabVIEW code in Fig. C.3 is used. Here, the code for sensors 2 and 3 is shown (representing the sensors in unit cells 2 and 3 of the metastructure, respectively), but the process remains the same for all sensors, including the optical sensor used to measure tip displacement z_{tip}. Because each sensor has two wires, the difference between the voltages of the two wires is taken as the sensor measurement. This is done to avoid ground loops, and is why the minus block is present before the sensor measurement is saved. Additionally, the Boolean "*Home Analog*" button observed in Fig. C.3, when true, is used to take the average of the sensor measurement, such as to reduce the background noise from the sensor and improve the quality of the measurement. Note how the contents of Fig. C.3 are within a while loop in LabVIEW. In the same loop, the code for acquiring the data of all the other sensors in the setup is also present.

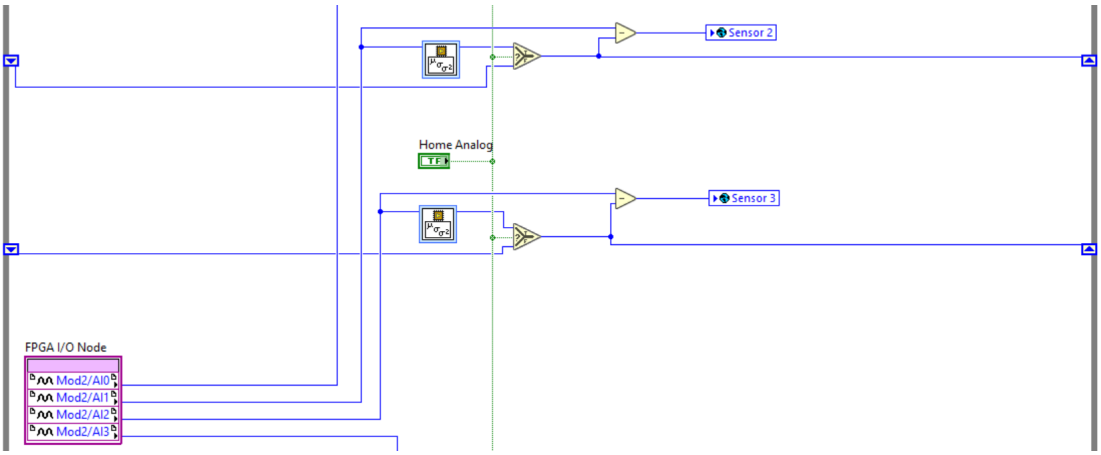

Figure C.3: How sensor data is obtained in the FPGA.vi file in LabVIEW.

The most important part of the FPGA.vi code is the part regarding the control loop. Here, as mentioned throughout the thesis, an individual control loop is established within each unit cell, where the sensor measurement is the input, and the actuator voltage is the output. Because all control loops are identical in the metastructure, a sub-VI is made for better clarity and visualisation within the code. The control loop sub-VI is illustrated in Fig. C.4, with all of

its input on the left-hand side, and its output on the right-hand side. Here, the sensor data is converted into fixed point representation (from 16-bit integer) to make the FPGA operations faster. The sensor value is then fed as the input of the controller ("*TF PPF 1*"), and the output signal is multiplied by a gain. When the Boolean "*PPF 1 on*" is false, the controller will not be used and the described steps will not be performed by the system. Instead, a zero value will be sent to the actuator. If the Boolean "*Sine input*" is true, the chirp disturbance generated in Fig. C.2 is sent to the actuator in the targeted unit cell. This is for identification purposes, of course. The output of the controller and the sinusoidal signal are then added using an addition block. This way, if desired, both "*PPF 1 on*" and "*Sine input*" Booleans can be true, and the collocated response of the system when the controller is active can be identified. If not, either of them can be true, and the system will function as explained. The offset and saturation blocks work in bits, as previously described in Fig. C.2, and are added as safety precautions in case of unstable controllers being implemented. The final output of the control loop is then fed to the collocated actuator, but is not shown in Fig. C.4 because this is the sub-VI. The actual system variables are added to the sub-VI in the FPGA.vi code.

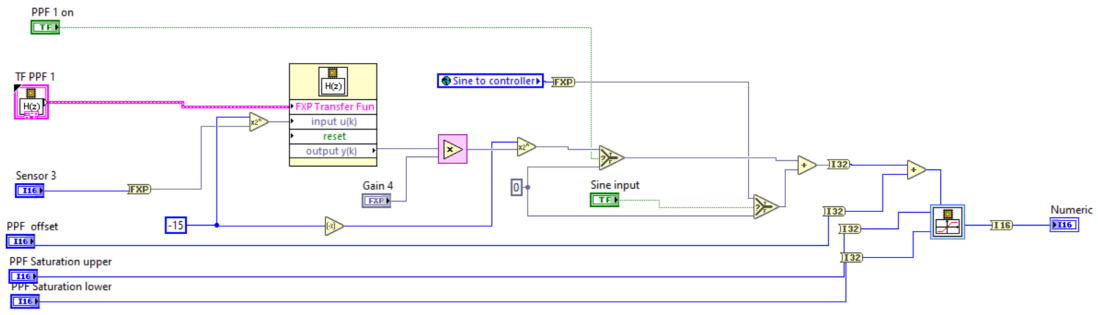

Figure C.4: Control loop sub-VI in the FPGA.vi file in LabVIEW.

The implementation of the created sub-VI block within the FPGA.vi is shown in Fig. C.5. This is fairly straightforward, as the variables specific to the targeted loop are inputted. This is done for each of the unit cells within the metastructure. In Fig. C.5, the variables for the first unit cell are shown.

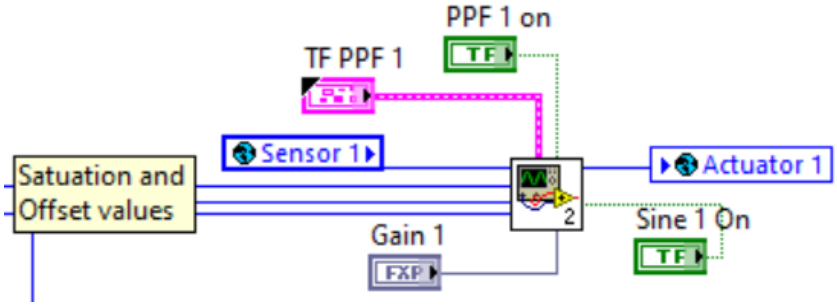

Figure C.5: Control loop VI connections in the FPGA.vi file in LabVIEW.

Within the FPGA.vi file, it is important for all of the variables to be written to FIFO. This is a data storage method used in LabVIEW, which means First In First Out. All of the data of

interest is built in an array, and saved in the FIFO such that it can then be opened in the other LabVIEW files. Fig. C.6 shows how the data is stored using FIFO after being put in an array.

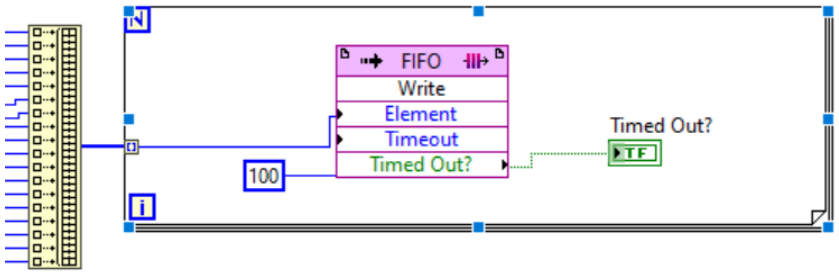

Figure C.6: FIFO in the FPGA.vi file in LabVIEW.

C.1.2 RTMain VI

In Fig. C.7, the front panel of the RTMain.vi file can be observed. Here, rapid control of the experimental setup is possible; the controllers of the different unit cells can be quickly turned on and off, and/or the sinusoidal disturbances can be sent to the actuators. The following list explains the function of all the parameters observed in Fig. C.7:

- **Starting Freq:** Defines the starting frequency of the sinusoidal disturbance. In this study, a value of 10 Hz was set.
- **Current Freq:** Defines the frequency at the current time step.
- **Increase Fraction:** At each step, the current frequency is multiplied (and hence increased) by the increase fraction. In this study, a value of 1.01 was set, implying an increase rate of 1%.
- **Max Freq:** Defines the maximum frequency of the sinusoidal disturbance. In this study, a value of 200 Hz was set.
- **Data Logging:** Boolean needs to be true if we want to log data to the Host.vi.
- **Reset sine:** Boolean needs to be true if the sinusoidal disturbance needs to be reset. If left on true, the sinusoid will not be sent. If left on false, the sinusoid will be sent.
- **Increase:** Boolean needs to be true so that the current frequency starts getting multiplied by the Increase Fraction.
- **Stack on:** Boolean needs to be true if the sinusoidal signal is desired on the stack actuator.

- **Sine *N* On:** Boolean needs to be true if the sinusoid signal is desired on the N-th actuator in the N-th unit cell.

- **PPF *N* On:** Boolean needs to be true if the controller in the N-th unit cell is desired to be operating.

- **Parameter Setting:** Defines the variables that can be changed for accurate tuning of the disturbance signals and actuator saturation limits.

- **Gain factor C*N*:** Value determines the gain by which the output of the N-th controller is multiplied by.

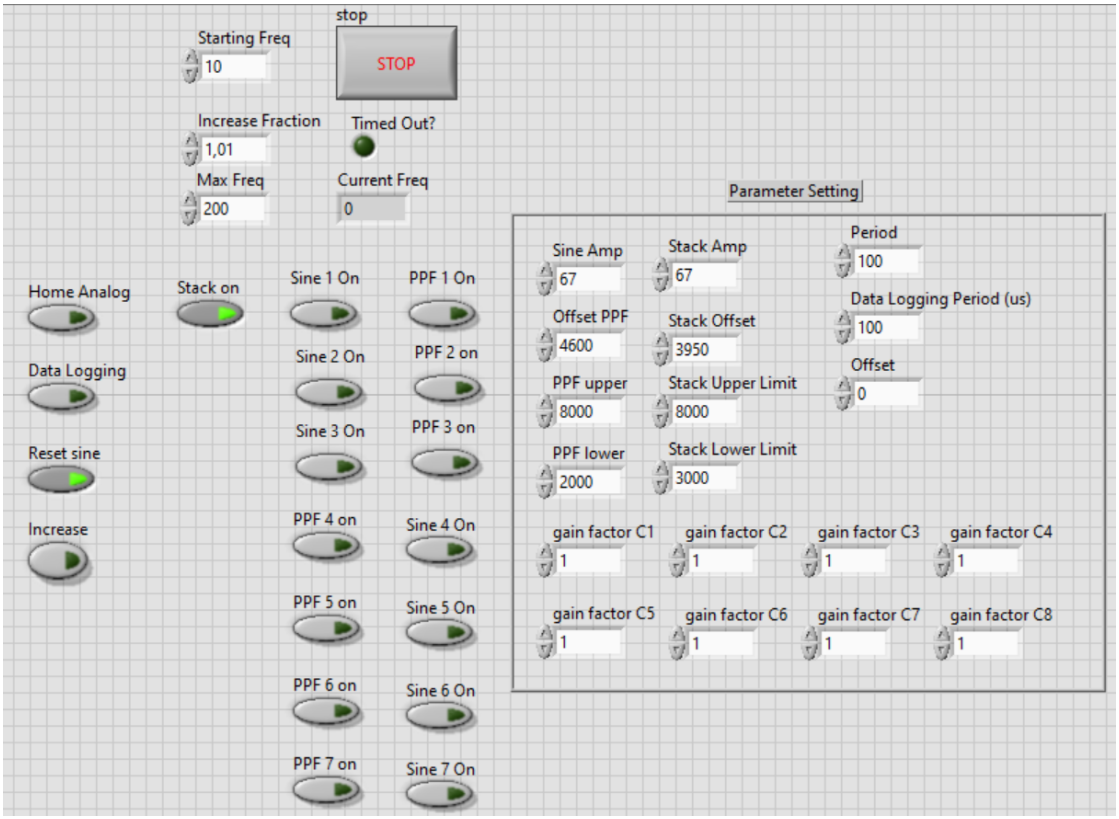

Figure C.7: Front panel of the RTMain.vi file in LabVIEW.

To implement the desired, tuned controllers within the unit cells of the metastructure, the coefficients in the RTMain.vi file need to be set. This is done in the block diagram of the RTMain.vi file, as shown in Fig. C.8. Here, only the numerator and denominator coefficients for the controller in unit cell 1 are shown, but the same code is present for each unit cell. It is extremely important to note that, in order for the correct coefficients to be implemented, the following few steps need to be followed:

1. Design the controller in MATLAB.

2. Discretise the controller. The '*tustin*' method was found to work appropriately.

3. Compare the discretised controller with the continuous controller to ensure they are the same in the region of interest.

4. Flip the coefficients of the controller from left to right, as LabVIEW imports coefficients in the opposite order compared to MATLAB. For instance, if num1 = [1, 2, 3] in MATLAB, they should be written [3, 2, 1] in LabVIEW.

5. In case of a decimal point in the controller coefficients, and a computer using Dutch settings, the dots (.) should also be changed to commas (,) in LabVIEW. For instance, if num1 = [1.5] in MATLAB, this should be written as [1,5] in LabVIEW.

The following code performs the outlined steps in a concise manner:

```
%% Extract numerator and denominator coefficients

C = 1; %Your tuned controller goes here!

Cd = c2d(C,ts,'tustin');

[numd, dend] = tfdata(Cd);

display(replace(join(fliplr(string(vpa(numd{:}))),' '),'.',','))

display(replace(join(fliplr(string(vpa(dend{:}))),' '),'.',','))

%% Compare discrete and continuous controllers

figure()
bode(Cd,C)
label('discrete controller','continuous controller')
grid on
```

Once all of this is done, the controller coefficients can be manually inputted in the RTMain.vi file to control the system.

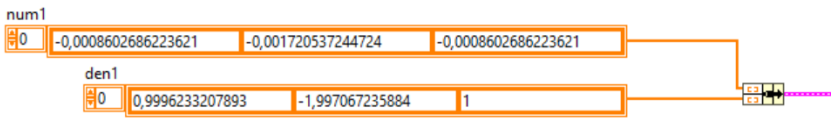

Figure C.8: Controller coefficients in the RTMain.vi file in LabVIEW.

C.1.3 Host VI

The Host.vi file is primarily used to observe and store the data from the experimental setup. Here, the front panel contains numerous waveform charts that display the measurements of the sensors and the signals sent to the actuators in real-time. An example is shown in Fig. C.9 for the first two unit cells. Of course, waveform charts for all sensors and actuators in the experimental setup are present in the complete front panel of the file. When the data is logged from the RTMain.vi file, the measurements are shown in white lines on the charts in the Host.vi file.

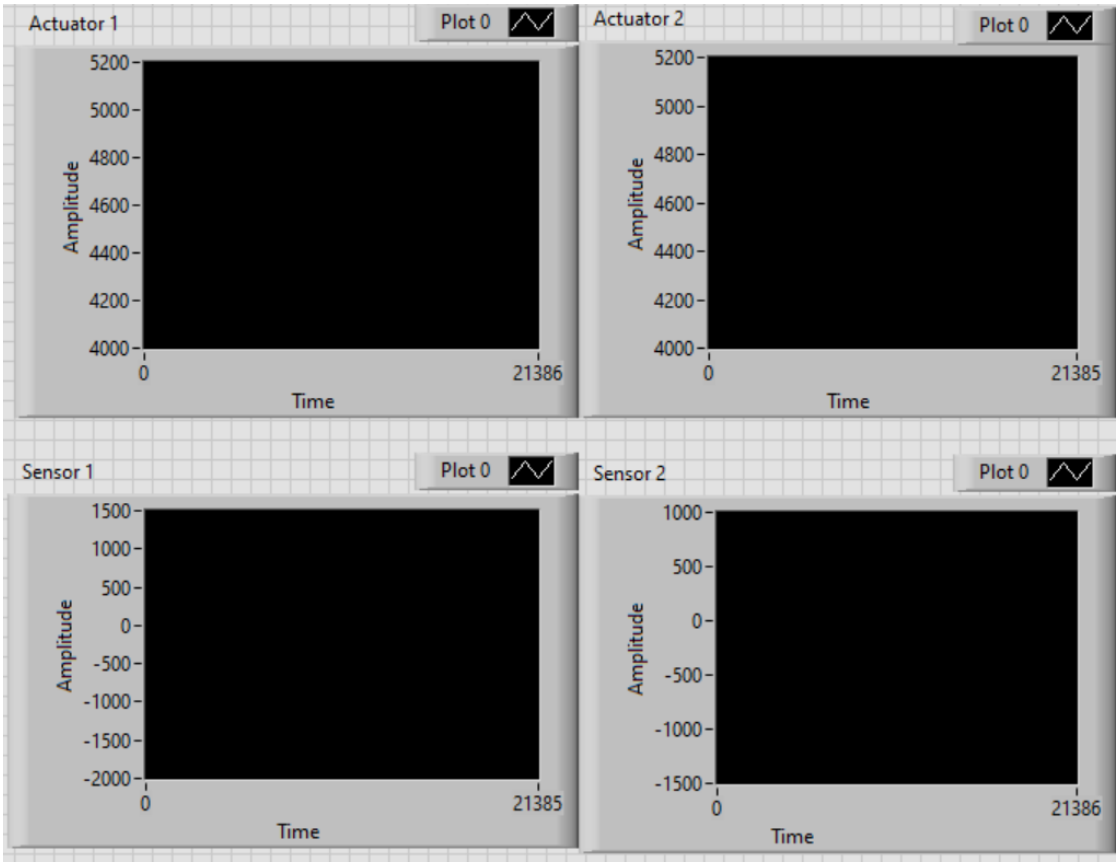

Figure C.9: Front panel of the Host.vi file in LabVIEW.

In the block diagram of the Host.vi file, instead, the data previously inputted to the FIFO (from the FPGA.vi file, recall Subsection C.1.1 and Fig. C.6) is read. The read data is then clustered into an array and saved to a measurement file. The specifications for the measurement file are shown in Fig. C.10. In the latter, the displayed settings were found to work well. Moreover, it is important to note that the data will be stored in the order in which it is sent to the FIFO in the FPGA.vi.

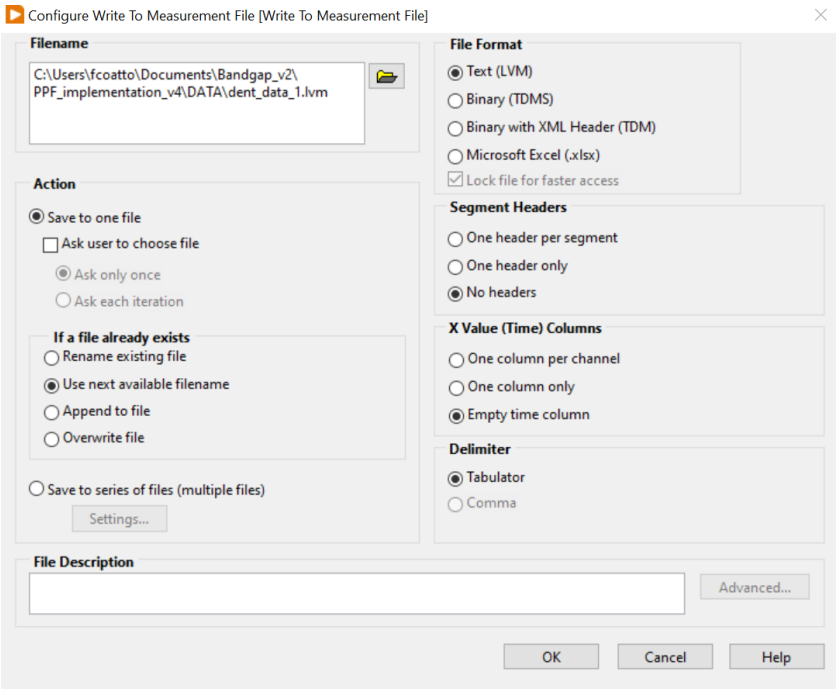

Figure C.10: Specifications for the measurement file in the Host.vi

C.2 Matlab post-processing of data

For post-processing the data acquired from the experimental setup in LabVIEW, this firstly needs to be imported in MATLAB. To do so, a few steps need to be followed in accordance with the settings specified in Fig. C.10. These are:

- Go to MATLAB Home and select "Import Data".
- Go to the file directory where the measurement file has been saved, and select it. In this case, from Fig. C.10, the directory is in the top-left corner.
- In the Import Menu, select "Column vectors" as Output Type.

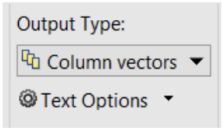

- Also select "Tab" as Column Delimiter.

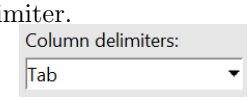

- Change variable names, if desired.
- Import the data into MATLAB.

The data imported can subsequently be used to plot transfer functions to observe the system

response. To do so, this needs to be converted into Frequency Response Data (FRD), such that the transfer function between the imported input and output can be plot. The following code can be used to plot the transfer function between two variables:

```
% Set sampling time as in LabVIEW code.

Fs = 1e4;

%Change variable names as desired:

input = d0ouble(VarName1);
output = double(VarName2);

% Hanning window is used in tfestimate for better identification:

L = length(input);
wind = hann(L/10);

% Create Frequency Response Data and estimate transfer function:

[G,f] = tfestimate(input,output,wind,[],[],Fs);
Gs = frd(G,2*pi*f,1/Fs);

% Observe the identified transfer function:

figure()
bode(Gs)
grid on
```

C.2.1 System Identification MATLAB Code

Because the experimental setup consists of 7 unit cells (i.e., 7 collocated actuators and sensors) as well as a sensor to measure tip displacement z_{tip} and a stack to excite the base of the beam, the full MIMO system will consist of an 8x8 system. To identify such a system, the sinusoidal chirp disturbance needs to be sent to each of the 8 actuators individually while all 8 sensors measure the recorded displacements. Then, all of the data needs to be imported in MATLAB, and the following code can be used to create a single FRD model with 8 outputs and 8 inputs. Such code is illustrated below:

```
%% Load all of the pre-saved, identified data:

load("act1.mat")
load("act2.mat")
load("act3.mat")
load("act4.mat")
load("act5.mat")
load("act6.mat")
load("act7.mat")
load("stack.mat")
```

```
% Set sampling time as in LabVIEW code.

Fs = 1e4;

%% Estimate the 8x8 transfer function system:

% Actuation using unit cell 1

[Hresp(1,1,:),freq] = tfestimate(act1,sen11,[],[],[],Fs);
Hresp(2,1,:) = tfestimate(act1,sen21,[],[],[],Fs);
Hresp(3,1,:) = tfestimate(act1,sen31,[],[],[],Fs);
Hresp(4,1,:) = tfestimate(act1,sen41,[],[],[],Fs);
Hresp(5,1,:) = tfestimate(act1,sen51,[],[],[],Fs);
Hresp(6,1,:) = tfestimate(act1,sen61,[],[],[],Fs);
Hresp(7,1,:) = tfestimate(act1,sen71,[],[],[],Fs);
Hresp(8,1,:) = tfestimate(act1,acc1,[],[],[],Fs);


% Actuation using unit cell 2

[Hresp(1,2,:)] = tfestimate(act2,sen12,[],[],[],Fs);
Hresp(2,2,:) = tfestimate(act2,sen22,[],[],[],Fs);
Hresp(3,2,:) = tfestimate(act2,sen32,[],[],[],Fs);
Hresp(4,2,:) = tfestimate(act2,sen42,[],[],[],Fs);
Hresp(5,2,:) = tfestimate(act2,sen52,[],[],[],Fs);
Hresp(6,2,:) = tfestimate(act2,sen62,[],[],[],Fs);
Hresp(7,2,:) = tfestimate(act2,sen72,[],[],[],Fs);
Hresp(8,2,:) = tfestimate(act2,acc2,[],[],[],Fs);


% Actuation using unit cell 3

[Hresp(1,3,:),freq] = tfestimate(act3,sen13,[],[],[],Fs);
Hresp(2,3,:) = tfestimate(act3,sen23,[],[],[],Fs);
Hresp(3,3,:) = tfestimate(act3,sen33,[],[],[],Fs);
Hresp(4,3,:) = tfestimate(act3,sen43,[],[],[],Fs);
Hresp(5,3,:) = tfestimate(act3,sen53,[],[],[],Fs);
Hresp(6,3,:) = tfestimate(act3,sen63,[],[],[],Fs);
Hresp(7,3,:) = tfestimate(act3,sen73,[],[],[],Fs);
Hresp(8,3,:) = tfestimate(act3,acc3,[],[],[],Fs);


% Actuation using unit cell 4

[Hresp(1,4,:),freq] = tfestimate(act4,sen14,[],[],[],Fs);
[Hresp(2,4,:),freq] = tfestimate(act4,sen24,[],[],[],Fs);
[Hresp(3,4,:),freq] = tfestimate(act4,sen34,[],[],[],Fs);
[Hresp(4,4,:),freq] = tfestimate(act4,sen44,[],[],[],Fs);
[Hresp(5,4,:),freq] = tfestimate(act4,sen54,[],[],[],Fs);
```

```
[Hresp(6,4,:),freq] = tfestimate(act4,sen64,[],[],[],Fs);
[Hresp(7,4,:),freq] = tfestimate(act4,sen74,[],[],[],Fs);
[Hresp(8,4,:),freq] = tfestimate(act4,acc4,[],[],[],Fs);


% Actuation using unit cell 5

[Hresp(1,5,:),freq] = tfestimate(act5,sen15,[],[],[],Fs);
[Hresp(2,5,:),freq] = tfestimate(act5,sen25,[],[],[],Fs);
[Hresp(3,5,:),freq] = tfestimate(act5,sen35,[],[],[],Fs);
[Hresp(4,5,:),freq] = tfestimate(act5,sen45,[],[],[],Fs);
[Hresp(5,5,:),freq] = tfestimate(act5,sen55,[],[],[],Fs);
[Hresp(6,5,:),freq] = tfestimate(act5,sen65,[],[],[],Fs);
[Hresp(7,5,:),freq] = tfestimate(act5,sen75,[],[],[],Fs);
[Hresp(8,5,:),freq] = tfestimate(act5,acc5,[],[],[],Fs);


% Actuation using unit cell 6

[Hresp(1,6,:),freq] = tfestimate(act6,sen16,[],[],[],Fs);
[Hresp(2,6,:),freq] = tfestimate(act6,sen26,[],[],[],Fs);
[Hresp(3,6,:),freq] = tfestimate(act6,sen36,[],[],[],Fs);
[Hresp(4,6,:),freq] = tfestimate(act6,sen46,[],[],[],Fs);
[Hresp(5,6,:),freq] = tfestimate(act6,sen56,[],[],[],Fs);
[Hresp(6,6,:),freq] = tfestimate(act6,sen66,[],[],[],Fs);
[Hresp(7,6,:),freq] = tfestimate(act6,sen76,[],[],[],Fs);
[Hresp(8,6,:),freq] = tfestimate(act6,acc6,[],[],[],Fs);


% Actuation using unit cell 7

[Hresp(1,7,:),freq] = tfestimate(act7,sen17,[],[],[],Fs);
[Hresp(2,7,:),freq] = tfestimate(act7,sen27,[],[],[],Fs);
[Hresp(3,7,:),freq] = tfestimate(act7,sen37,[],[],[],Fs);
[Hresp(4,7,:),freq] = tfestimate(act7,sen47,[],[],[],Fs);
[Hresp(5,7,:),freq] = tfestimate(act7,sen57,[],[],[],Fs);
[Hresp(6,7,:),freq] = tfestimate(act7,sen67,[],[],[],Fs);
[Hresp(7,7,:),freq] = tfestimate(act7,sen77,[],[],[],Fs);
[Hresp(8,7,:),freq] = tfestimate(act7,acc7,[],[],[],Fs);


% Actuation using stack actuator

[Hresp(1,8,:),freq] = tfestimate(stack,sen1p,[],[],[],Fs);
[Hresp(2,8,:),freq] = tfestimate(stack,sen2p,[],[],[],Fs);
[Hresp(3,8,:),freq] = tfestimate(stack,sen3p,[],[],[],Fs);
[Hresp(4,8,:),freq] = tfestimate(stack,sen4p,[],[],[],Fs);
[Hresp(5,8,:),freq] = tfestimate(stack,sen5p,[],[],[],Fs);
[Hresp(6,8,:),freq] = tfestimate(stack,sen6p,[],[],[],Fs);
```

```
[Hresp(7,8,:),freq] = tfestimate(stack,sen7p,[],[],[],Fs);
[Hresp(8,8,:),freq] = tfestimate(stack,accp,[],[],[],Fs);



%% Create the 8x8 FRD model:

H = frd(Hresp,2*pi*freq,1/Fs);

%% Visualise results:

% Performance channel:

figure(1)
bode(H(8,8))

% Collocated channel for unit cell 1:

figure(2)
bode(H(1,1))
```

Notice how with this code the performance channel is located in position (8, 8) of the MIMO system, whereas the collocated channel for unit cell 1 is located in position (1, 1). The identification results can be visualised in the following appendix section.

Appendix D

System Identification

In this appendix chapter, the results of the system identification are shown. The experimental setup of Appendix A is used and the process outlined in Appendix C is followed.

D.1 Collocated Transfer Functions

In this section, the transfer functions identified in the collocated channels of the experimental setup are shown.

Collocated Transfer Function: Actuator 1 - Sensor 1 (Unit Cell 1)

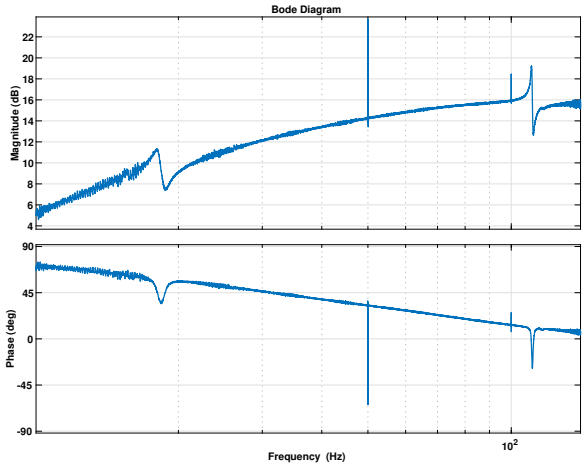

Figure D.1: Collocated transfer function for unit cell 1 of the metastructure.

Collocated Transfer Function: Actuator 2 - Sensor 2 (Unit Cell 2)

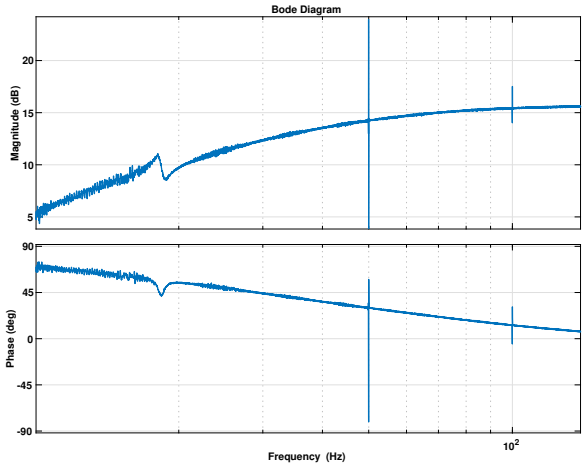

Figure D.2: Collocated transfer function for unit cell 2 of the metastructure.

Collocated Transfer Function: Actuator 3 - Sensor 3 (Unit Cell 3)

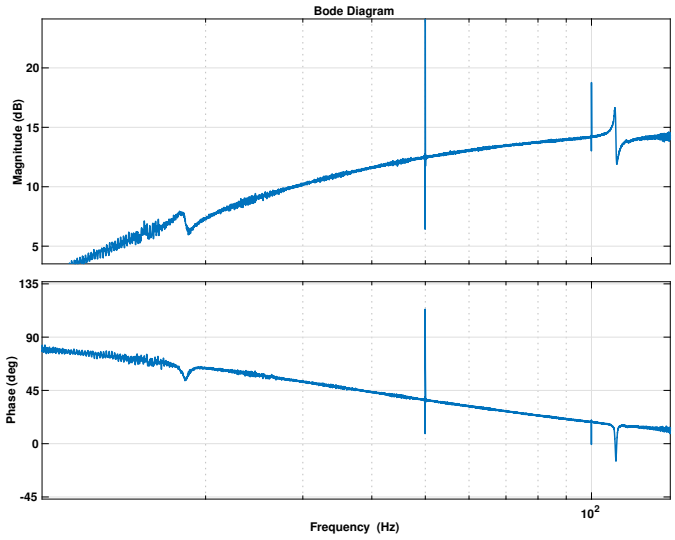

Figure D.3: Collocated transfer function for unit cell 3 of the metastructure.

Collocated Transfer Function: Actuator 4 - Sensor 4 (Unit Cell 4)

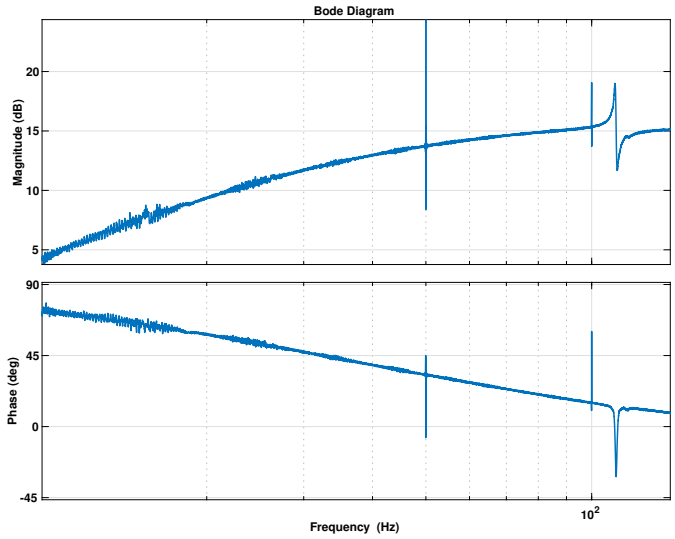

Figure D.4: Collocated transfer function for unit cell 4 of the metastructure.

Collocated Transfer Function: Actuator 5 - Sensor 5 (Unit Cell 5)

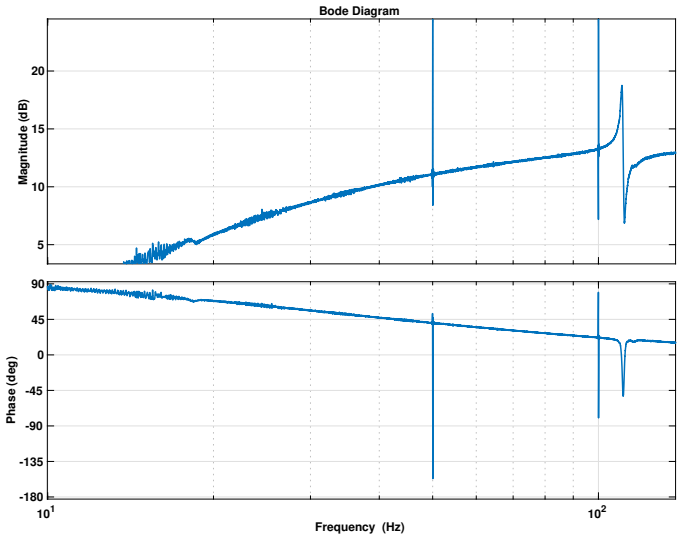

Figure D.5: Collocated transfer function for unit cell 5 of the metastructure.

Collocated Transfer Function: Actuator 6 - Sensor 6 (Unit Cell 6)

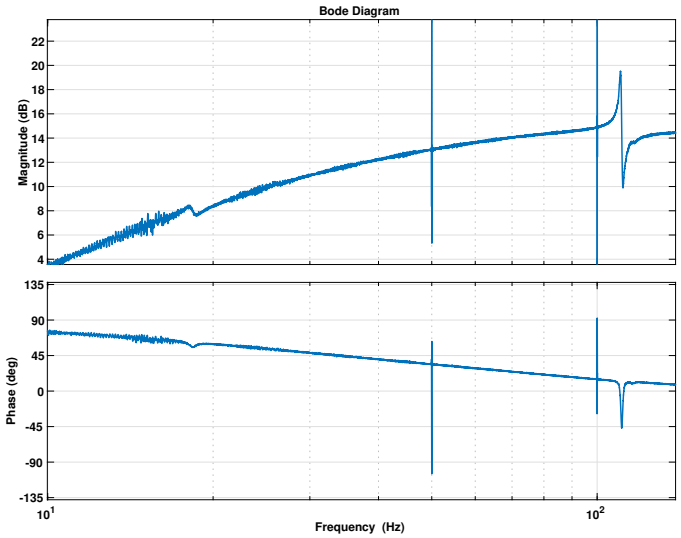

Figure D.6: Collocated transfer function for unit cell 6 of the metastructure.

Collocated Transfer Function: Actuator 7 - Sensor 7 (Unit Cell 7)

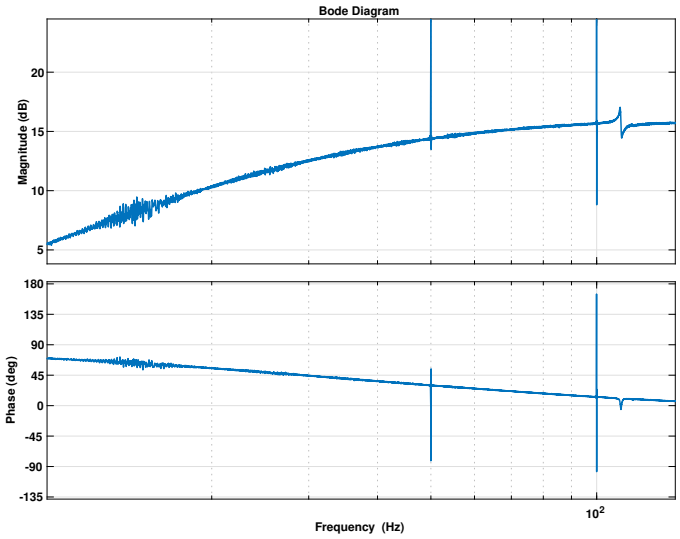

Figure D.7: Collocated transfer function for unit cell 7 of the metastructure.

D.2 Performance Transfer Function

In this section, the transfer function identified in the performance channel of the experimental setup is shown.

Performance Transfer Function: Stack - Position sensor

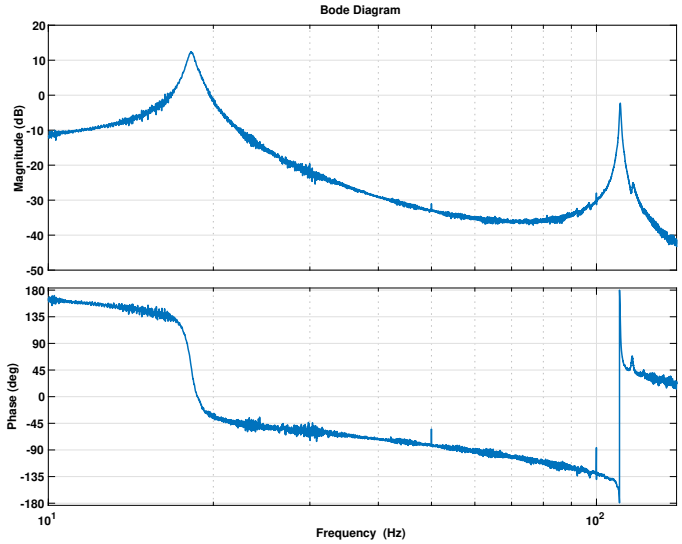

Figure D.8: Performance transfer function for the metastructure.

D.3 MIMO System Identification

In this section, the complete identified MIMO plant for the experimental setup is shown. Here, the phase plots are not illustrated for clarity. Moreover, in Fig. D.9, the columns represent the control inputs, from left to right: V_{a1}, V_{a2}, V_{a3}, ..., V_{a7}, F_z. The rows, instead, represent the system outputs, from top to bottom: V_{s1}, V_{s2}, V_{s3}, ..., V_{s7}, z_{tip}. Hence, the transfer function in position (1, 1) represents the transfer function from V_{a1} to V_{s1}. Similarly, the transfer function in position (8, 8) represents the transfer function from F_z to z_{tip}. Likewise, the transfer function in position (6, 3) represents the transfer function from V_{a6} to V_{s3}, and so on. This is all in accordance with the MATLAB code and process outlined in Appendix C.

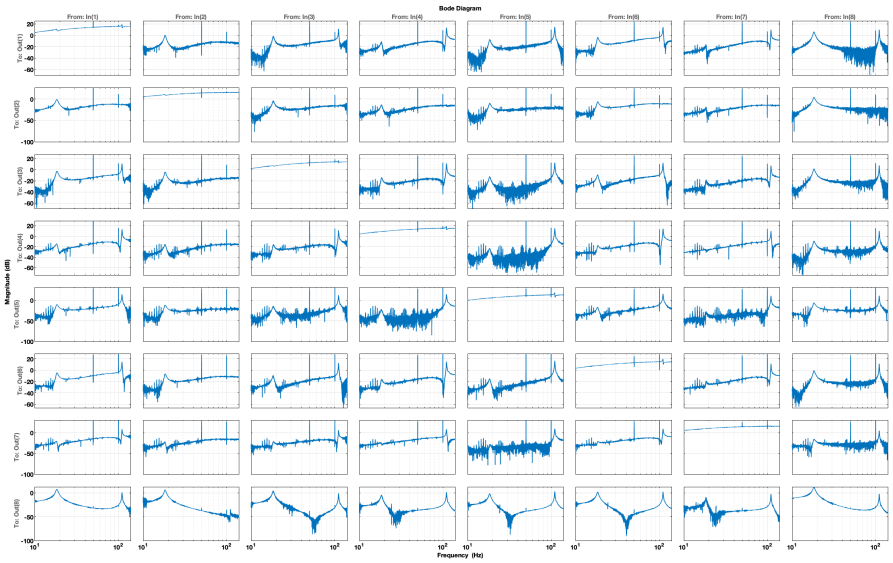

Figure D.9: MIMO plant for the metastructure.